UNIVERSIDADE FEDERAL DE SANTA CATARINA
CENTRO TECNOLÓGICO
DEPARTAMENTO DE AUTOMAÇÃO E SISTEMAS

Brian Silvério Pscevozniki

End of Course Project

Gas shielding fixture for laser welding of metallic bipolar plates

Aachen

2025

Brian Silvério Pscevozniki

Gas shielding fixture for laser welding of metallic bipolar plates

Thesis submitted to the Federal University of Santa Catarina as an approval requirement to the Control and Automation Engineering course discipline **DAS5511: Projeto de Fim de Curso**
Supervisor: Regis Henrique Gonçalves e Silva

Aachen

2025

Brian Silvério Pscevozniki

Gas shielding fixture for laser welding of metallic bipolar plates

This internship report was evaluated in the context of the DAS5511 course: Projeto de Fim de Curso and **APPROVED** in its final form by the Control and Automation Engineering Course.

Aachen, 2025-08-04

Regis Henrique Gonçalves e Silva
Advisor
Universidade Federal de Santa Catarina

Apoorva Nagarkar
Company Supervisor
Fraunhofer Institute for Production Technology IPT

DISCLAIMER

Aachen, August fifth, 2025.

As representative of the Fraunhofer Institute for Production Technology in which the present work was carried out, I declare this document to be exempt from any confidential or sensitive content regarding intellectual property, that may keep it from being published by the Federal University of Santa Catarina (UFSC) to the general public, including its online availability in the Institutional Repository of the University Library (BU). Furthermore, I attest knowledge of the obligation by the author, as a student of UFSC, to deposit this document in the said Institutional Repository, for being it a Final Program Dissertation ("*Trabalho de Conclusão de Curso*"), in accordance with the *Resolução Normativa n° 126/2019/Cun.*

Florian Hüsing

Digital unterschrieben von Florian Hüsing
Datum: 2025.08.08 13:59:19 +02'00'

Florian Hüsing

Department Head Modular Production Machines

Fraunhofer Institute for Production Technology

Abstract

Laser welding has emerged as a critical joining method for manufacturing bipolar plates used in proton exchange membrane fuel cells (PEMFCs). These components demand high precision, mechanical integrity, and chemical stability, yet welding-induced oxidation remains a persistent challenge that compromises weld quality. This work presents the design, simulation, and experimental validation of customized Shielding gas supply structure aimed at mitigating oxidation during the laser welding process. A series of masks for localized shielding were iteratively developed using CAD modeling and evaluated through Computational Fluid Dynamics (CFD) simulations in ANSYS Fluent to optimize flow uniformity and reduce stagnation zones. Three design iterations were fabricated using additive manufacturing and tested under controlled conditions with varying argon flow rates. Optical microscopy, Scanning Electron Microscopy (SEM), and Energy Dispersive X-ray Spectroscopy (EDX) were used to assess surface oxidation, weld morphology, and internal oxygen content. The results demonstrate that the final design iteration (Mask 2 V3) achieved significantly improved gas retention and weld integrity, particularly at a flow rate of 12 L/min. Nonetheless, the study also highlights persistent asymmetries linked to the external gas feeding system, emphasizing the importance of holistic system integration. This research provides insight into the interplay between fluid dynamics and weld quality in precision manufacturing applications.

Keywords: LBW process gas, oxidation, bipolar plates, CFD simulation, SEM, EDX, hydrogen fuel cells.

Resumo

A soldagem a laser tornou-se um método de união essencial na fabricação de placas bipolares utilizadas em células a combustível de membrana de troca de prótons (PEMFCs). Esses componentes exigem alta precisão, integridade mecânica e estabilidade química, mas a oxidação durante o processo de soldagem continua sendo um desafio recorrente que compromete a qualidade das juntas. Este trabalho apresenta o projeto, simulação e validação experimental de uma estrutura personalizada de proteção a gás desenvolvidas especificamente para mitigar a oxidação durante a soldagem a laser. Uma série de máscaras de proteção localizada foi desenvolvida iterativamente por meio de modelagem CAD e avaliada com simulações de Dinâmica dos Fluidos Computacional (CFD) no ANSYS Fluent, com o objetivo de otimizar a uniformidade do fluxo e reduzir zonas de estagnação. Três iterações do projeto foram fabricadas por manufatura aditiva e testadas sob condições controladas, com diferentes vazões de argônio. Microscopia óptica, Microscopia Eletrônica de Varredura (MEV) e Espectroscopia por Dispersão de Energia (EDX) foram utilizadas para avaliar a oxidação superficial, a morfologia da solda e o conteúdo de oxigênio nas seções transversais. Os resultados demonstram que a iteração final do projeto (Máscara 2 V3) obteve melhorias significativas na retenção de gás e na integridade da solda, especialmente com uma vazão de 12 L/min. No entanto, o estudo também evidencia assimetrias persistentes associadas ao sistema externo de alimentação de gás, ressaltando a importância de uma abordagem integrada do sistema. Esta pesquisa contribui para a compreensão da relação entre dinâmica de fluidos e qualidade da solda em aplicações de manufatura de alta precisão.

Palavras-chave: soldagem a laser, proteção gasosa, oxidação, placas bipolares, simulação CFD, MEV, EDX, células a combustível de hidrogênio.

List of Figures

Contents

1 Introduction

Hydrogen fuel cells represent a critical technology in the global transition towards sustainable energy systems. Among their core components, bipolar plates play a pivotal role in managing gas distribution, electrical conduction, and thermal management within the fuel cell stack. As the demand for more efficient, durable, and cost-effective fuel cells grows, so does the need to refine the manufacturing processes associated with these components. Laser welding has emerged as a promising technique for assembling thin metallic bipolar plates due to its precision, speed, and potential for automation. However, one of the primary challenges associated with this method is oxidation during the welding process, which can compromise both the mechanical integrity and chemical stability of the joint.

Oxidation occurs when molten metal at the weld interface reacts with atmospheric oxygen, leading to the formation of oxide layers that degrade the weld quality. Traditional methods of gas shielding, such as simple nozzles or inert gas chambers, often fail to provide sufficient coverage or control, especially for complex or miniaturized components, and/or are difficult to integrate in the welding cell. To address this, the development of more effective and localized gas shielding solutions is essential. This thesis focuses on the design, simulation, and experimental validation of customized gas shielding structures intended to minimize oxidation during the laser welding of metallic bipolar plates.

The approach undertaken combines iterative CAD-based design with computational fluid dynamics (CFD) simulations to optimize the internal geometry and gas distribution of these shielding gas supply structures. Successive prototypes were fabricated using additive manufacturing and tested under controlled welding conditions, with performance assessed through optical and electron microscopy, as well as compositional analysis. The findings presented herein contribute to a deeper understanding of the interplay between shielding gas behavior, structural design, and weld quality, offering actionable insights for improving industrial welding processes in fuel cell production.

2 Theoretical Basis

2.1 Hydrogen Fuel Cells: Overview and Architecture

Hydrogen fuel cells are electrochemical devices that convert chemical energy stored in hydrogen and oxygen into electrical energy, with water and heat as byproducts. Unlike combustion-based energy systems, fuel cells operate without hydrocarbon fuels, making them highly efficient and environmentally friendly. Their application spans various sectors including transportation, stationary power generation, and portable power devices, owing to their scalability and clean operation (CARRETTE; FRIEDRICH; STIMMING, 2000).

Fuel cells are categorized into several types based on their electrolyte material and operating temperature. According to (CARRETTE; FRIEDRICH; STIMMING, 2000), the most prominent types include:

- **Proton Exchange Membrane Fuel Cells (PEMFCs):** Operate at low temperatures (85 - 105°C) and use a solid polymer membrane as the electrolyte. They are favored in automotive and portable applications due to their quick startup and high power density.
- **Solid Oxide Fuel Cells (SOFCs):** Operate at high temperatures (500 - 1000°C) using a ceramic electrolyte. These are suited for stationary power generation and cogeneration systems due to their high efficiency and fuel flexibility.
- **Alkaline Fuel Cells (AFCs):** Use an aqueous alkaline solution as the electrolyte. They offer high performance but are sensitive to CO_2 contamination, which limits their use in open environments.
- **Phosphoric Acid Fuel Cells (PAFCs):** Typically used in large-scale stationary applications, these operate at intermediate to high temperatures and provide good electrical efficiency.

A typical fuel cell stack consists of multiple repeating units, each comprising several key components:

- **Bipolar Plates:** Serve to distribute reactant gases (hydrogen and oxygen/air) across the electrodes, collect current, and manage thermal and water flow.
- **Membrane Electrode Assembly (MEA):** Consists of a proton-conductive membrane sandwiched between a cathode and anode. This is where the electrochemical reactions occur.

- **Gas Diffusion Layers (GDLs):** Positioned between the electrodes and the flow fields, these facilitate uniform gas distribution and water management.
- **Sealing Materials:** Prevent leakage of gases and ensure safe operation under pressure and thermal cycling.

The performance and durability of the fuel cell stack depend critically on the precision and quality of these components.

2.2 Bipolar plates

The Bipolar Plates (BPP) used in this project are meant for hydrogen fuel cells. According to (HERMANN; CHAUDHURI; SPAGNOL, 2005), these cells will be economically important in the near future for automotive propulsion applications, stationary power generation, portable power and industrial applications due to their sustainability and versatility. The Proton Exchange Membrane Fuel Cell (PEMFC) is an electrochemical device that produces electrical and thermal energy through chemical reaction. A schematic of PEMFC is illustrated in Figure 1.The main components of the PEMFC include a bipolar plate (BPP), gas diffusion layer (GDL), catalyst layer (CL), and proton exchange membrane (PEM). On the anode side, hydrogen coming from the anode flow field first passes through the anode GDL and is finally converted into hydrogen ions and electrons at the anode CL. The anodic reaction is as in eq. 2.1.

$$H^2 \rightarrow 2H^+ + 2e^- \quad E_a^0 = 0V \tag{2.1}$$

The H^+ ions produced at the anode penetrate through the proton exchange membrane to the cathode. At the cathode, the O_2 fed through the cathode flow field first passes the cathode GDL. There, it reacts with the protons to form water at the cathode CL. The produced water exists as a gas-liquid two-phase mixture. Part of this water is consumed to maintain proton conductivity in the PEM, while the rest is discharged through the flow field. The cathodic reaction is as in eq. 2.2.

$$\frac{O_2}{2} + 2e^- + 2H^+ \rightarrow H_2O \quad E_c^0 = 1.23V \tag{2.2}$$

Combining equations 2.1 and 2.2 the overall expression is as in eq. 2.3.

$$H_2 + \frac{O_2}{2} \rightarrow H_2O \quad E^0 = 1.23V \tag{2.3}$$

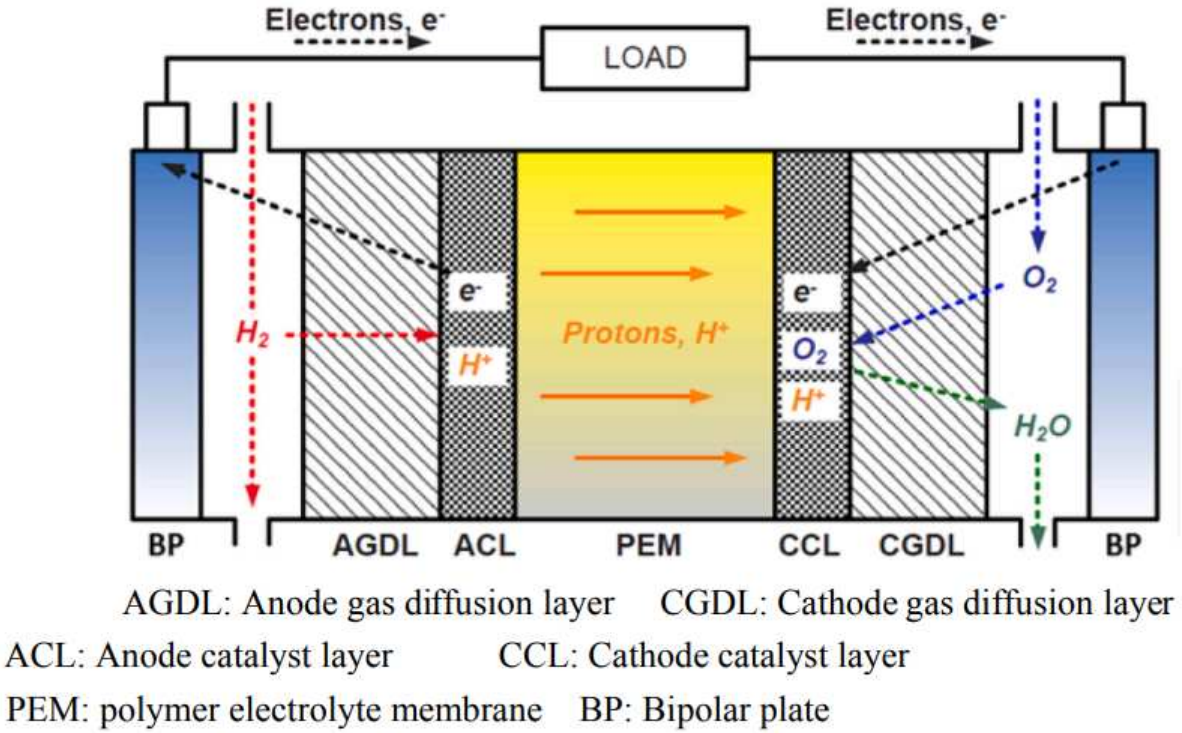

Figure 1 – PEM schematic

Source: (XIONG et al., 2021)

Bipolar plates play a crucial role in the operation of a PEMFC. They facilitate the flow of electrical current between cells, regulate water and heat within the cell, and create channels for the reactant gases, namely hydrogen and oxygen. In the design of PEM hydrogen fuel cells, bipolar plates are manufactured in large quantities; for this reason, it is important that these plates are made from materials that allow efficient manufacturing and are compatible with automated high-volume and cost-effective production processes, as noted by (TAWFIK; HUNG; MAHAJAN, 2007).

(XIONG et al., 2021) defined the following characteristics for the bipolar plate:

- The bipolar plate serves as the structural support of the PEMFC, requiring sufficient mechanical strength to sustain the MEA. Materials with high specific strength are preferred to increase power density;
- Its surface contains the flow fields for gas and water transport, so it must be compatible with precise and scalable manufacturing processes;
- It is also responsible for current collection, making high electrical conductivity essential;
- To prevent mixing of the oxidant and the fuel, low gas permeability is required;

- Due to the acidic environment of the electrolyte, the plate must resist chemical and electrochemical corrosion to ensure durability;
- Thermal conductivity must be high, and thermal expansion low, to tolerate operating temperatures around 80°C;
- Lastly, for commercial viability, the plate must be low-cost and suitable for mass production.

(BORUP; VANDERBORGH, 1995) and (MEHTA; COOPER, 2003) defined numerical criteria a material must meet to be appropriate for this application:

- Electrical conductivity: plate resistance $< 0.01\Omega cm^2$.
- Thermal conductivity: as high as possible.
- Hydrogen/gas permeability: $< 10^{-4}$ cm^3/s cm^2.
- Corrosion resistance: corrosion rate < 0.016 mA/cm^2.
- Compressive strength: > 1550 g/cm^2.
- Density: < 5 g/cm^2.

The materials researched up to this date are classified into three categories: non-metals, such as non-porous graphite or electrographite; metals, both coated and non-coated; and composites, which encompass polymer-carbon and polymer-metal combinations. Figure 2 shows the classification of materials used to manufacture bipolar plates.

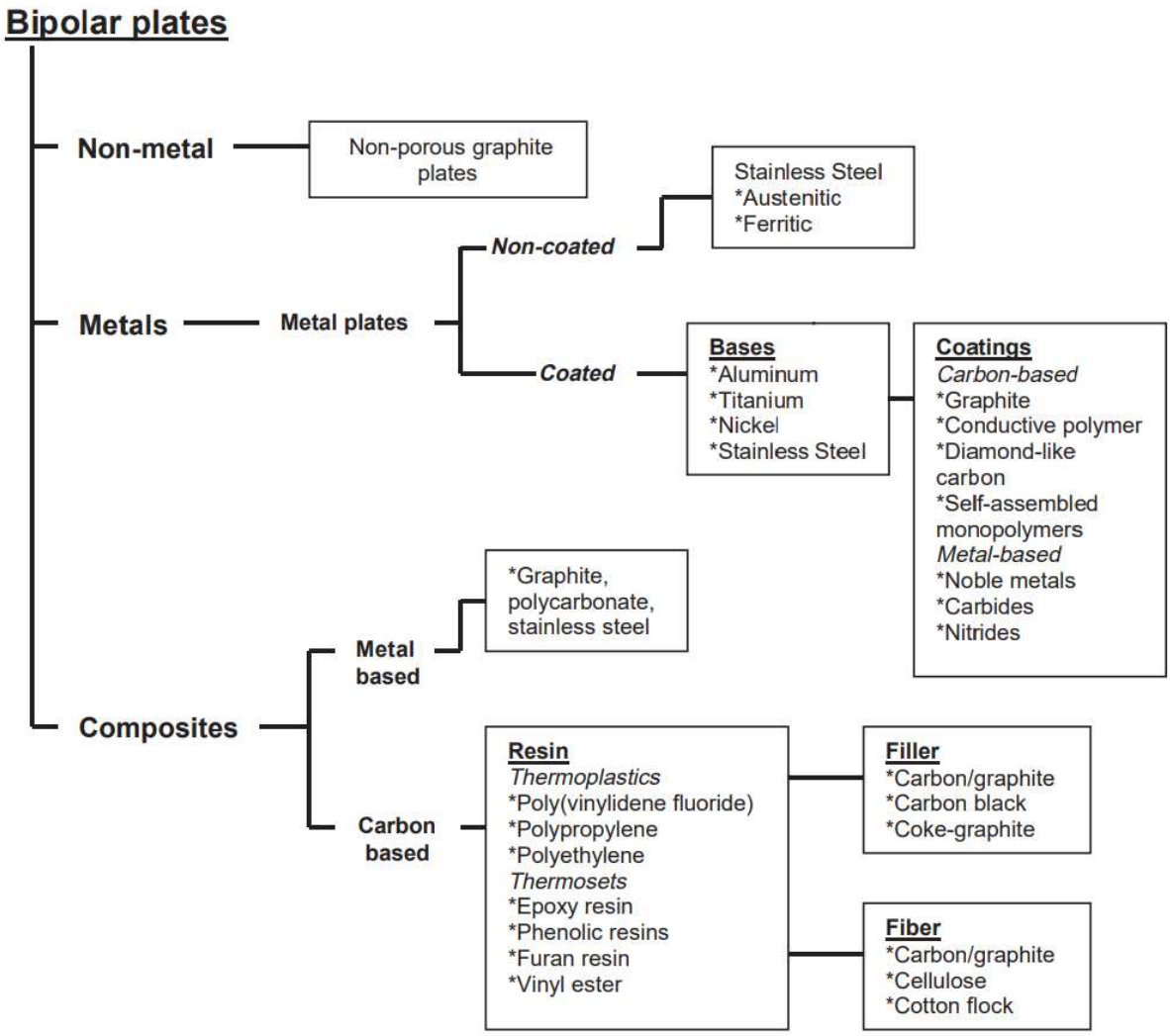

Figure 2 – BPP materials classification

Source: (HERMANN; CHAUDHURI; SPAGNOL, 2005)

2.2.1 Non-porous graphite

According to (HERMANN; CHAUDHURI; SPAGNOL, 2005) and (TAWFIK; HUNG; MAHAJAN, 2007), graphite is the traditional material used for BPPs, due to their excellent properties of low surface contact resistance, high corrosion resistance, and chemical stability; therefore, they survive the fuel cell environment. They also show very low resistivity, allowing for optimal electrochemical power output. However, these materials have certain significant drawbacks concerning brittleness, gas permeability, high cost, and low mechanical strength.

A more recent article (SONG et al., 2020) explains some of the manufacturing methods investigated to meet the economic and operating standards for the viability of this material in a real-world application. Generally, the non-porous graphite plates are produced by a high-temperature graphitization treatment of carbon or graphite powder

with graphitized resin. The graphitization demands a temperature greater than 2500°C, through a very accurate heating. It is a very time-consuming process. The evaporation of impurities during graphitization results in new pores, producing leakage in PEM fuel cells and reducing the concentration of reaction gases, which consequently deteriorates the performance of the cell and stack. Additional treatments are required to reduce porosity and improve surface quality. However, graphite plates are more susceptible to fracturing during manufacturing compared to other types of bipolar plates.

Due to the low strength and brittle nature of the graphite plates, the manufacture of ultra-thin bipolar plates with less than 1.5mm thickness cannot be realized through machining. The process has high friction between the cutting tool and graphite, which impairs the dimensional precision and surface finish. The machining of the gas flow channel in the bipolar plate further increases the production cost, so this technique has been phased out.

In an effort to reduce the high costs associated with machining, injection molding has also been utilized to fabricate bipolar plates. Adding metal powders to the mixture increases conductivity, while adding carbon or ceramic fibers improves mechanical strength. However, there are many disadvantages to injection molding. The binder removal times can go up to seven days, thick sections crack, and the size can't exceed diameters above 3 cm. The process is also prone to knit lines, short shots, flashing, sink marks, and thermal strains. Graphitization can further enhance the performance of the plates but at great expense and, hence, cannot be used in injection molding if the intention is mass production.

Gelcasting, also referred to as aqueous tape casting, is a technique of net-shape fabrication initially developed in the United States by the Oak Ridge National Laboratory to manufacture high-quality ceramic components of complex geometrical shapes. In recent years, the technology has been expanded to create parts from carbon, composite, and metal materials. Compared to injection molding, the parts manufactured through gelcasting indicated considerable improvement in mechanical properties, electrical conductivity, and surface quality.

2.2.2 Non-coated metals

Metal sheets are considered promising candidates for bipolar plate material, as they have excellent mechanical stability, electrical and thermal conductivity, and are easily stamped into desired shapes in flow channels. However, in the operating environment of a fuel cell, characterized by a pH of 2-3 and temperatures around 80°C, metal plates are susceptible to corrosion and dissolution. The freed metal ions from corrosion may contaminate the proton exchange membrane, reducing its ionic conductivity. In addition, the corrosion layer on the BPP surface would lead to an increase in electrical resistance, negatively affecting cell performance. To tackle the problems described above, research

has been done with two kinds of metallic plates: non-coated and coated with protective layers. Metals used for this purpose are aluminium, stainless steel, titanium, and nickel (HERMANN; CHAUDHURI; SPAGNOL, 2005).

(TAWFIK; HUNG; MAHAJAN, 2007) noted that stainless steel with high concentrations of (Cr) is the best choice for BPPs for its high corrosion resistance. Cr in the alloy forms a passive film on the surface of stainless steel. Corrosion resistance improves as the chromium content increases, however, a thick non-conductive Cr_2O_3 passive layer can develop, leading to undesirably high surface contact resistance.

In their research, (WANG; TURNER, 2004) had also targeted stainless steel samples such as AISI434, AISI436, AISI441, AISI444, and AISI446. They presented the results on passivation of AISI446 in both anode and cathode simulated PEM fuel cell environments with highly stable passive film growth on their surface. However, there was an increase in interfacial contact resistance (ICR) between steel and carbon backing material due to the passive film.

The thickness of the passive film on AISI446 was estimated at 2.6 nm when formed at 0.1 V in a simulated anodic environment and 3.0 nm when formed at 0.6 V in a simulated cathodic environment. Modifying the chromium oxide-dominated passive film may improve ICR, as ICR increased after passivation, according to the authors. XPS depth profiling revealed that the air-formed surface films contained both iron oxides and chromium oxides, but none of them dominated. Passive films developed in the fuel cell environment mainly consisted of Cr oxide, with iron oxides playing a minor role. Also, the passive film on the cathode was found to be thicker than that on the anode, which resulted in higher ICR at the cathode.

2.2.3 Coated Metals

According to (TAWFIK; HUNG; MAHAJAN, 2007), in metallic bipolar plates, corrosion protection is attained by applying a thin coating layer. Such coatings should be electrically conductive, strongly bonded to the base metal, and ensure very good protection against corrosive environment attacks. For better performance and to avoid micro-pores and cracks due to unequal expansion, the thermal expansion coefficients of the base metal and the coating should be as close as possible. Some coating techniques may result in defects such as pinholes, and the search for reliable coating techniques for bipolar plates is still a field of active research.

Two big categories of coatings have been considered so far: carbon-based and metal-based. Graphite, conductive polymers, diamond-like carbon, and organic self-assembled monolayers are involved in the category of carbon-based coatings. Noble metals, metal nitrides, and metal carbides are included in the category of metal-based coatings. Table 1

represents a summary of studied coating materials.

Table 1 – Coatings

Coating method	Coating materials	Coating processes	Base plate materials			
			Al	SS	Ti	Ni
Conductive polymers coating	Conductive polymers	Not specified	Not specified			
Diamond-like carbon coating	Diamond-like carbon	Not specified	Not specified			
Gold topcoat layering	Gold over nickel over copper	Pulse current electrodeposition	x			
Graphite foil layering	(1) Sublayer - sonicated graphite particles in an emulsion, suspension or paint (e.g. graphite particles in an epoxy resin thinned by an organic solvent, such as toluene); (2) topcoat - exfoliated graphite in the form of sheets of flexible, graphite foil	Painting OR pressing	x		x	x
Graphite topcoat layering	(1) Sublayer - titanium over titanium–aluminum-nitride; (2a) overcoat - transient metal sublayer of Cr (Ti, Ni, Fe, Co) followed by sulfuric/chromic acid OR; (2b) topcoat - graphite	PVD (closed-field, unbalanced, magnetron sputter ion plating) and chemical anodization/oxidation overcoating	x	x	x	x
Indium doped tin oxide layering	Indium doped tin oxide (Sn(In)O2)	Electron beam evaporation		x		
Lead oxide layering	(1) Sublayer - lead; (2) topcoat - lead oxide (PbO/PbO2)	Vapor deposition and sputtering		x		
Organic monopolymer coating	Organic self-assembled monopolymers	Not specified	Not specified			
Silicon carbide layering	(1) n-Type silicon carbide (SiC); (2) gold	Glow discharge decomposition and vapor deposition		x		
Stainless steel layering	(1) Sublayer - chromium/nickel/molybdenum-rich stainless steel OR nickel–phosphorus alloy; (2) topcoat-titanium-nitride	Physical vapor deposition (PVD)	x	x	x	
Titanium–aluminum-nitride layering	Titanium–aluminum-nitride layer	RF-planar magnetron (sputtering)	x			
Titanium-nitride layering	Titanium-nitride (TiN) layer	RF-diode sputtering			x	

Source: (TAWFIK; HUNG; MAHAJAN, 2007)

The coefficient of thermal expansion (CTE), corrosion resistance, and micro-pore or crack appearance of the coating are some critical issues to protect bipolar plates from the harsh PEM fuel cell environment. Though PEM fuel cells normally work below 100°C, during normal driving conditions, temperature cycling between 75°C and 125°C occurs frequently in start-up and shutdown operations in a vehicle application. Large mismatches in the CTE between substrate and coating material can lead to coating failure. One remedy for this is the application of intermediate coating layers whose CTE values are intermediate between those of adjacent layers.

2.2.4 Composites

A composite plate is a plate made of composite materials, such as resin and fiber. According to (HERMANN; CHAUDHURI; SPAGNOL, 2005), polymer composites are a good choice of material for a bipolar plate due to their lightweight and mold capability into various shapes and sizes, which is highly desirable in PEM fuel cell stacks. Composite plates can be classified into either metal-based or carbon-based.

Los Alamos National Laboratory developed a metal-based BPP composite using a combination of porous graphite, polycarbonate plastic, and stainless steel. This design takes advantage of the relative ease and lower cost of producing porous graphite compared to non-porous graphite. The impermeability of the plate is achieved through the stainless steel and polycarbonate components. Stainless steel adds structural rigidity, while the graphite provides corrosion resistance. Polycarbonate contributes to chemical resistance and can be molded into complex shapes to accommodate gaskets and manifolds. This layered composite plate is, from both a stability and cost point of view, a promising alternative for bipolar plate applications.

Carbon composite bipolar plates are fabricated using thermoplastic resins such as polypropylene, polyethylene, and poly(vinylidene fluoride), or thermosetting resins such as phenolics, epoxies, and vinyl esters. These materials are combined with fillers and may include fiber reinforcement.

2.3 Laser welding and gas shielding

According to (KATAYAMA, 2013), welding is one of the most versatile methods for joining materials and is widely used across various industries. Laser welding, which utilizes a laser as a high-power-density heat source, is considered as an advanced technique for joining materials. The laser beam's power density, comparable to that of an electron beam, far exceeds that of arc plasma. This high density can create a deep narrow keyhole during welding, enabling the production of deep and narrow penetration welds with precision and efficiency. Conduction welding, or melt in, is also possible, whereby a shallow weld pool is produced. Keyhole formation is dependent on welding parameters such as laser power, welding speed, and material properties.

Laser welding is capable of joining a wide range of metals and plastics, from very thin sheets as small as 0.01 mm to thick plates up to 50 mm in thickness (KATAYAMA, 2013). Altough the process can be carried out without controlled surrounding environments, process assist gases like Ar, He, N_2 have proven to yield superior quality of weld seams. It is highly regarded for its ability to deliver high-quality, precise, and reliable joints with excellent performance, speed and flexibility during the process, and minimal distortion on the material. Laser based welding process can be integrated into automated manufacturing setups, reducing the requirement of manuel processing. As advancements in laser technology and joining techniques continue, the applications of laser welding are expanding rapidly, solidifying its role as a leading joining method in modern manufacturing. On the other hand, laser beam welding (LBW) faces challenges its implementation and operation. Due to the small nature of the beam and focus, joint preparation and alignment, as well as the machanization/robotization system shall yield high precision, robustness and repeatability.

Laser welding can be applied across a broad range of scales, generally categorized into two domains: macro-welding and micro-welding. This distinction reflects differences in application size, energy input, and precision requirements, and plays a key role in determining the appropriate process configuration (KATAYAMA, 2013) and (STEEN, 2010). Macro-welding typically involves the joining of large components or thick sections of material where deeper penetration and higher mechanical strength are needed. In this context, keyhole mode welding is commonly used due to its ability to generate deep, narrow welds through localized vaporization and stable keyhole formation. These processes usually rely on continuous wave lasers, particularly high-power fiber or CO_2 lasers, and operate with higher energy densities to ensure robust structural joints. Macro-welding is widely used in automotive, aerospace, and heavy manufacturing applications, where long, uninterrupted weld seams and high throughput are essential.

Micro-welding, in contrast, focuses on the precise joining of small or delicate components, often using lower laser power and highly controlled energy delivery. Conduction mode welding is predominant in these scenarios, as it minimizes heat input and avoids keyhole formation, thereby reducing thermal distortion and preserving material integrity. Pulsed lasers, particularly diode, Nd:YAG, or low-power fiber lasers, are frequently used in micro-welding due to their ability to deliver short, controlled bursts of energy. These systems are essential in applications such as medical device fabrication, microelectronics, and fine instrumentation, where accuracy and minimal heat-affected zones are critical.

Ultimately, whether a laser welding process is applied to macro- or micro-welding depends not on the laser type alone but on how the process is configured. Factors such as power output, mode of operation (continuous or pulsed), focusing optics, and material thickness determine the suitability of the method for large-scale structural welding or precision microjoining tasks.

As noted by (DU et al., 2023), micro-welding differs from macro-welding in that at least one dimension of the weld is less than 100 μm. In the early applications of laser micro-welding, the low power of laser sources necessitated the use of a pulsed laser and a focusing lens to achieve material melting. More recently, advanced laser welding systems incorporating high-power lasers and scanning galvanometers have been introduced for micro-welding. Compared to earlier systems, the scanning galvanometer enhances welding speed and precision while also reducing the heat-affected zone.

In thermal conduction welding, the laser energy is absorbed only at the surface, producing shallow, wide welds with aspect ratios typically below 1. In contrast, penetration welding is characterized by keyhole formation within the melt pool, which dramatically increases laser energy absorption, from around 10-30% in conduction mode to over 80% in stable keyhole mode, due to multiple internal reflections within the vapor cavity (STEEN, 2010). This results in weld seams with much higher aspect ratios, often exceeding 5. A

transitional regime exists between these two modes, in which conduction and penetration alternate irregularly, producing a mixed-mode welding process. (DU et al., 2023) demonstrated that effective gas shielding suppresses this transient phase, suggesting that instability in keyhole formation, driven by oxidation at the weld pool surface, is responsible for the fluctuation between modes.

In (DU et al., 2023), the authors performed tests in AISI304 stainless steel foils with dimensions of 20 mm × 100 mm × 0.1 mm. A single-mode fibre laser (IPG-YLS3000) operating at a wavelength of 1.07 μm and capable of delivering up to 3 kW of power serves as the laser source. The module provides a laser power of 500 W, adjustable within a range of 30 W to 500 W. The welding setup includes a galvanometer system featuring a 354 mm focal length and a focal spot diameter of 70 μm. The laser power varies between 30 to 80 W and the welding speed from 5 to 60 mm/s.

Initially, laser micro-welding is conducted using a shielding gas, argon. Figure 3(a) displays the surface and cross-sectional views of the welds produced with laser power ranging from 30 W to 80 W at a welding speed of 40 mm/s. The weld seams are consistently continuous and uniform, demonstrating a stable welding process in the presence of shielding gas. The cross-sectional images reveal that full penetration welding is achieved at laser powers exceeding 50 W. Furthermore, comparable weld seams are observed across different welding speeds.

To better understand the formation of the transient phase, laser micro-welding is also carried out without the use of shielding gas. Figure 3(b) presents the surface and cross-sectional views of the welds. Both weld seams, created at a relatively low laser power of 30 W and a high laser power of 80 W, appear continuous and uniform. However, the width of the weld seam varies irregularly when the laser power is between 30 W and 80 W, suggesting an unstable welding process within this power range. Full-penetration welding is achieved at laser powers above 50 W, indicating that the instability occurs during penetration welding. Notably, the dark surfaces of the welds reveal oxidation during laser welding without gas protection, in contrast to the gas-protected welds, which highlights the importance of shielding gas for oxidation prevention.

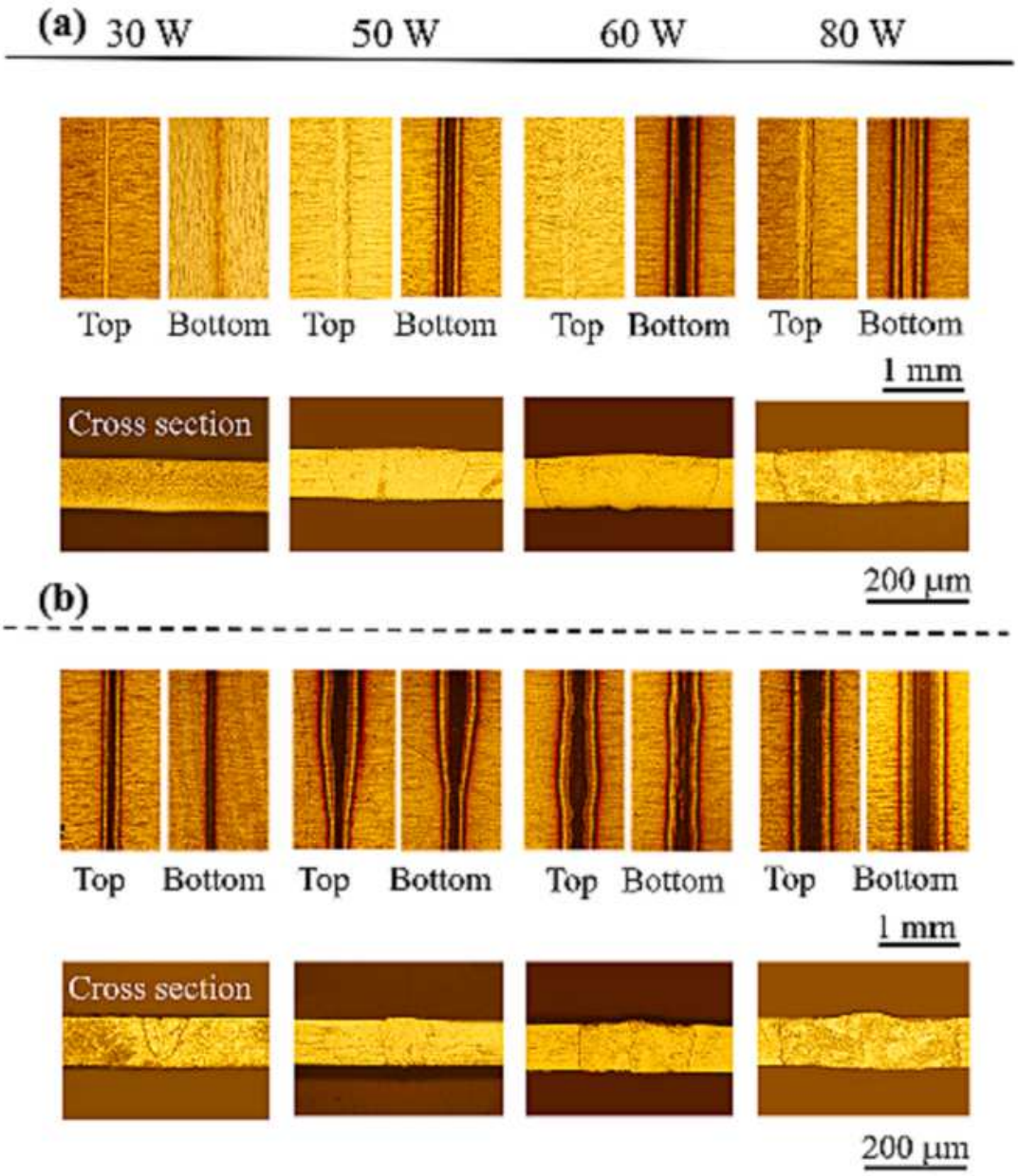

Figure 3 – Images of weld surface and cross-section with varying laser powers (a) with shielding gas (b) without shielding gas

Source: (DU et al., 2023)

Most welding processes rely on shielding gases to protect the weld surface and surrounding area from atmospheric contamination. Maintaining the correct shielding gas flow rate is crucial for achieving high-quality welds. Insufficient flow can lead to defects such as porosity in the solidified weld or oxidation. Research has demonstrated that both the composition and flow rate of the shielding gas significantly impact the appearance and quality of the final weld, (CAMPBELL et al., 2013).

(CAMPBELL et al., 2013) also explains that the optimal shielding gas flow rate depends on the welding process, operating parameters, welding orientation, and gas

composition. In a draught-free environment, a flow rate of 6 l/min can produce high-quality welds. However, in Gas Metal Arc Welding (GMAW), flow rates of 15–18 l/min are commonly used. A common misconception is that higher gas flow improves weld quality, leading some to set flow rates as high as 25 l/min. However, research shows that at flow rates exceeding approximately 23 l/min, turbulence can occur in the shielding gas column, drawing atmospheric gases into the weld region and potentially causing defects in the solidified weld. Although a different process, these concepts for Arc Welding can also be considered and applied for laser micro-welding. One fundamental difference is that, in laser welding, the shielding gas can be used also to displace or hinder the formation of plasma, reducing the interaction of the beam with plasma, thus raising process efficiency.

2.4 Measuring and evaluation methods

In the context of oxidation measurement of a welded surface, some processes are more prominent. Most weld characterization researches use optical microscopes for preliminary analysis. Optical microscopes are the oldest and most simple design of microscopes. The image amplification in this microscope works by using a basic physical concept, light refraction. Light travels slower in glass than it does in the air, causing a light refraction; by using a properly designed curved glass lens, the microscope generates a virtual amplified version of a real object, (GANDHI, 2019).

Microscopes may incorporate multiple lenses for higher amplification and can be used to identify surface-level characteristics in a material, as used in the research conducted by (SHIRINZADEH-DASTGIRI et al., 2015). In this research, using an optical Olympus microscope, model BX60-USA, the authors identified ferrite and pearlite microstructures and the existence of cracks in the welded joints of AISI 1518 low carbon steel pipes. With this information, they successfully identified a failed sample for further analysis with more in-depth methods.

Optical microscopy by itself can, as explained, only identify surface-level characteristics. For a better understanding of the oxidation spread in a structure, cross section techniques may be applied. Cross section is, once again, a simple process to explain. It consists of cutting slices of a sample that, after some careful treatment, may be analysed with microscopy. This technique is used by (WOLTERSDORF et al., 1995) in conjunction with a JEOL-JEM 1000 electron microscope to observe the bonded weld between aluminium and glass ceramics. In the research they observed the defects in the joining process, such as cracks and micropores, as well as crystallization phenomena and oxidation.

This same research also applies another method to determine the chemical composition of the amorphous interlayer, Energy Dispersive X-ray Spectrometry (EDXS), on the same cross section pieces. According to (NEWBURY; RITCHIE, 2013), EDXS technology

works by analysing the X-ray emitted in the interaction of electron beams and a sample. With this technique it is possible to identify most elements of the periodic table, except for hydrogen, helium and lithium. With EDXS, (WOLTERSDORF et al., 1995) identified the composition of the interlayer as 50 to 60% Al and 40 to 50% oxygen, so it could be applied to determine how a shielding gas used during welding impacts the oxidation process.

2.5 CFD and Flow Regime

In this work, Computational Fluid Dynamics (CFD) plays a critical role in evaluating and optimizing the gas distribution behavior within the custom shielding structures. The objective of the simulations was to ensure uniform and stable coverage of argon over the weld surface, minimizing the risk of oxidation during the laser welding process. To achieve this, the internal volume of the shielding structure was discretized and solved numerically using the Navier-Stokes equations, allowing the prediction of velocity fields, pressure gradients, and flow behavior (ASHGRIZ; MOSTAGHIMI, 2002).

In ANSYS Fluent, the governing equations for fluid flow are solved using the finite volume method (FVM), where the computational domain is divided into small control volumes, and the integral form of the conservation equations is applied to each one. Fluent calculates fluxes across the faces of each control volume and uses iterative solvers to resolve the continuity, momentum, and, if enabled, energy equations throughout the domain. Depending on the expected flow regime, various numerical schemes and physical models, such as laminar or turbulent flow models, can be selected. For this study, a steady-state, pressure-based solver with second-order spatial discretization was employed under the assumption of laminar flow, which is appropriate given the relatively low Reynolds numbers involved (INC., 2023).

A fundamental consideration in gas flow design is the classification of the flow regime, specifically whether the flow is laminar or turbulent. Laminar flow is characterized by smooth, orderly motion of fluid particles, resulting in more predictable and uniform gas distribution. Turbulent flow, on the other hand, is dominated by chaotic eddies and mixing, which can cause fluctuations in shielding effectiveness and local pressure zones that lead to incomplete coverage or recirculation near the weld interface (ASHGRIZ; MOSTAGHIMI, 2002).

The flow regime in internal passages such as those in the shielding mask can be estimated using the Reynolds number (Re), defined as:

$$Re = \frac{\rho v D}{\mu} \tag{2.4}$$

where ρ is the gas density, v is the flow velocity, D is the hydraulic diameter of

the channel, and μ is the dynamic viscosity. For argon at room temperature and small channel dimensions (on the order of a few millimeters), laminar flow typically corresponds to $Re < 2300$ (MUNSON, 2010). In this project, inlet velocities were set around 1.98 m/s, with channel diameters between 4 mm and 5 mm, resulting in Reynolds numbers generally below this threshold, justifying the assumption of laminar flow conditions in most regions.

2.6 Shielding Gas Dynamics and Nozzle Design Principles

The shielding gas, typically argon or helium, serves to displace atmospheric gases such as oxygen and nitrogen from the weld zone, creating an inert environment that preserves the chemical and mechanical properties of the welded joint. The efficiency of this protection depends not only on the type and flow rate of the shielding gas but also significantly on the geometry of the nozzle or shielding structure through which the gas is delivered (KOU, 2003). In the case of laser welding, it may also influence the formation of laser induced plasma plume.

The dynamics of shielding gas flow are governed by fluid mechanics principles, where nozzle shape, orientation, and exit velocity influence how the gas disperses over the weld area. Ideally, the gas should form a stable and uniform coverage over the molten pool without inducing turbulence that might entrain atmospheric gases. Nozzles with gradual transitions, such as conical or diffuser shapes, promote laminar flow and minimize flow separation at the exit (KATAYAMA, 2013). In contrast, abrupt changes in geometry or sharp internal features can trigger vortices and stagnation zones, reducing shielding effectiveness (CAMPBELL et al., 2013).

Flow velocity also plays a critical role. Insufficient velocity may fail to clear ambient air effectively, while excessive velocity can induce turbulence and disrupt the molten pool. The optimum velocity range varies depending on nozzle dimensions and standoff distance but generally aims to maintain Reynolds numbers within the laminar regime for stable coverage (KATAYAMA, 2013).

Studies have shown that diffuser-type geometries, where the gas expands in a controlled manner before exiting, help achieve more even flow distribution and reduce the risk of localized gas starvation (KATAYAMA, 2013). Rounded internal corners, as opposed to sharp angles, further support smooth flow transition and reduce pressure loss within the delivery system.

3 Problem description and requirements

A critical issue in the laser welding of metallic bipolar plates is the formation of oxidation on the top surface of the weld seam, precisely where the laser beam directly impacts the plate. During the welding process, this area is fully exposed to ambient air and elevated temperatures generated by the laser, leading to rapid oxidation. Figure 4 shows a weld seam without the application of shielding gas, and the oxidation is identifiable by the yellow and blue colorization. The oxidation is visible and measurable, adversely affecting surface quality, electrical conductivity, corrosion resistance, and, potentially, the mechanical integrity of the bipolar plates (YANG; LOU; GE, 2024).

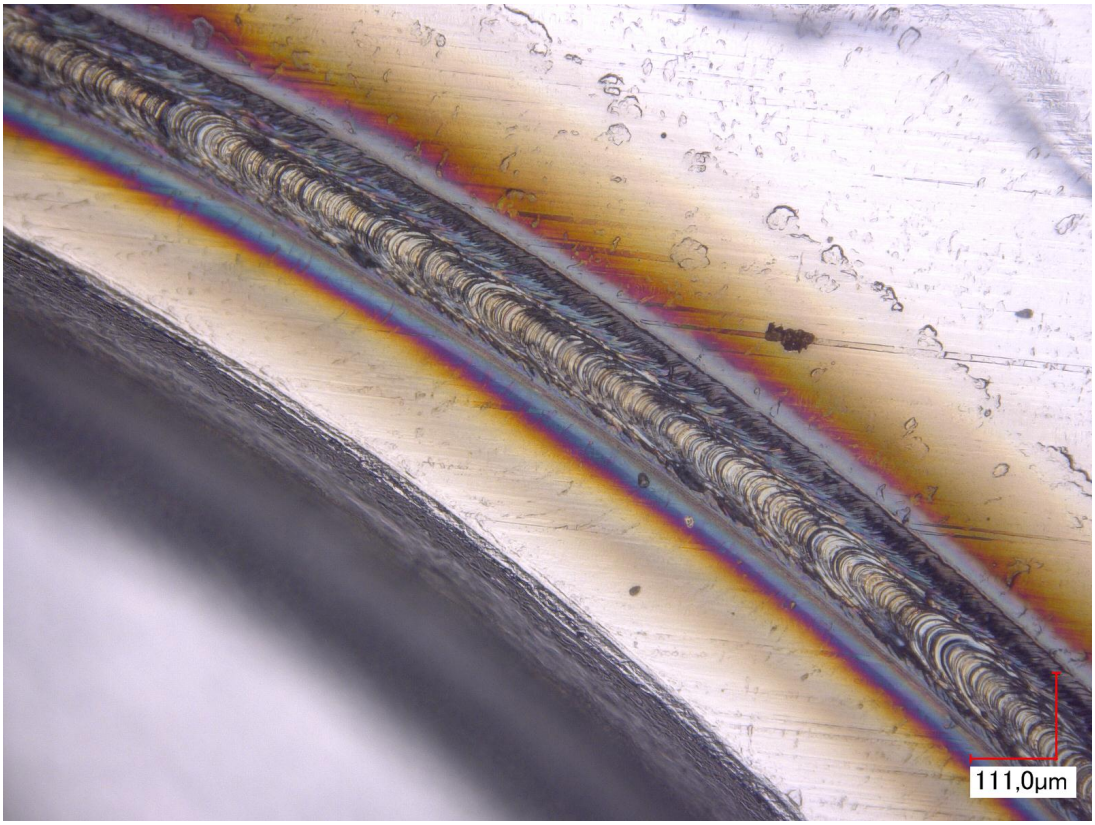

Figure 4 – Weld seam without the usage of proper gas shielding

Source: Author

The approach to mitigating oxidation used in the process involved supplying inert shielding gas, argon, from beneath the welding fixture and through a specifically designed structure placed above the weld surface. The approach was selected because standard delivery systems fail to provide adequate shielding coverage of the directly exposed laser interaction zone. The result is inconsistent protection, as the argon coverage is uneven

or insufficient, allowing oxygen ingress at critical welding locations. This inadequacy is primarily due to turbulence, stagnation zones, or inefficient flow distribution inherent in conventional gas shielding configurations, (CHO et al., 2012), (SCHRICKER; BAUMANN; BERGMANN, 2021).

Increasing the argon gas flow rate as a remedy is impractical, inefficient, and costly, offering limited improvements while significantly increasing gas consumption. Thus, a specialized, efficient, and localized shielding gas supply solution is necessary. Such a solution must deliver uniform, laminar flow of inert gas directly over the top weld surface without interfering with the laser path, welding equipment, or clamping mechanisms. Additionally, the design must ensure minimal gas consumption to remain economically viable and scalable for industrial applications. This research, therefore, addresses the need for a targeted, optimized gas shielding structure capable of effectively minimizing oxidation on the top surface of the bipolar plates during laser welding, thereby enhancing weld quality, reducing post-processing efforts, and improving overall production efficiency and product reliability.

3.1 Requirements

To effectively address the oxidation problem identified on the upper surface of metallic bipolar plates during laser welding, the shielding gas supply solution developed in this research must satisfy several essential requirements. Primarily, the solution must significantly reduce or entirely prevent the visible oxidation occurring at the weld zone directly impacted by the laser beam. The effectiveness of this protection should be verifiable through optical microscopy and cross-sectional analysis of weld seams, ensuring that minimal or no detectable oxide layers form.

Achieving consistent and uniform gas flow is critical, therefore, the shielding structure must deliver laminar flow distribution of inert gas (argon) across the entire targeted welding region. This uniformity is necessary to eliminate the possibility of localized stagnation zones or turbulent flow patterns, which would otherwise allow oxygen to penetrate and compromise shielding efficiency. Flow uniformity results achieved from CFD simulation should be verified using experimental validation.

The designed shielding system must also be fully compatible with existing industrial setups. It must integrate seamlessly within current welding fixtures, ensuring no interference with the laser beam path, clamping equipment, or other critical components. Precise dimensional conformity and ease of integration into the welding environment are essential, and compatibility must be confirmed through practical testing within operational setups.

Furthermore, to ensure economic viability and practicality in high-volume manufacturing environments, the shielding solution must minimize gas consumption. It should

operate effectively at lower inert gas flow rates than conventional industrial standards, reducing operational costs without compromising protective performance. Experimental verification comparing gas flow rates and oxidation prevention effectiveness will serve to confirm this requirement.

Operational convenience is also a critical requirement. The shielding system must be easy to assemble, disassemble, and adapt between production runs or plate configurations, thus minimizing downtime and facilitating rapid transitions between different production batches. Practical assembly tests will serve to assess the convenience and ease of use of the designed structure. Clear, quantifiable performance metrics should be established for all aspects of this design, enabling ongoing evaluation and iterative improvements based on standardized quality assessments and reproducible test results.

4 Proposed solution and implementation

This chapter introduces the proposed solution and its implementation, detailing the iterative design process used to improve gas shielding performance during laser welding of metallic bipolar plates. Beginning with an evaluation of the baseline geometry, each subsequent iteration incorporates simulation-driven modifications aimed at optimizing internal gas flow and reducing oxidation. This chapter outlines the rationale behind each design change, the simulation procedures used for validation, and the practical steps taken to fabricate and test the manufactured prototypes under controlled welding conditions.

4.1 Simulation Setup

To evaluate the gas distribution within the shielding structures, a series of Computational Fluid Dynamics (CFD) simulations were performed. The internal flow volumes of each gas shielding mask were extracted from the respective SolidWorks models and exported as Parasolid files. These volumes were then imported into ANSYS Workbench for preprocessing.

A structured mesh was generated with a global element size of 0.01 m, while the regions corresponding to the inlets and outlets were refined using face sizing of 0.001 m to capture detailed flow characteristics near the boundary conditions. The physics preference was set to CFD, and the solver preference was configured for ANSYS Fluent.

Inlet and outlet boundaries were defined explicitly within the Workbench environment prior to exporting the mesh to ANSYS Fluent for further simulation. This setup enabled accurate modeling of the internal gas dynamics under various design and flow rate conditions used throughout the iterative design process.

4.2 Iteration 1 - Baseline Design

The baseline design serves as the initial reference from which all subsequent improvements and iterations were derived. Initially, the original SolidWorks design files and a welded bipolar plate fabricated using this design were provided. The original design, referenced as Mask 1 V1 and Mask 2 V1, is presented in the technical drawing appendix (Drawing: Mask 1 V1 and Drawing: Mask 2 V1).

Pre trials for Identification of problem area in the existing system were carried out.

Parallel to the experimental examination, Computational Fluid Dynamics (CFD) simulations were conducted utilizing ANSYS Fluent. These simulations evaluated the argon

gas distribution within the original shielding gas structure at various inlet velocities ranging from 0.04 m/s to 0.1 m/s. Contrary to expectations, variations in the inlet velocities had negligible influence on gas distribution quality. Ultimately, these lower velocities failed to adequately protect the weld surface, demonstrating little variation in results and revealing substantial oxidation zones. Consequently, the final implemented solution reverted to a much higher inlet velocity of 1.98 m/s (corresponding to approximately 12 L/min gas flow rate).

A critical evaluation of the baseline design highlighted several structural and functional issues:

- **Sharp internal curves:** These contributed significantly to turbulence and inefficient gas flow, resulting in uneven gas distribution across the welding surface.
- **Inefficient smaller inner tubes:** These tubes did not substantially enhance gas distribution and were therefore identified as unnecessary for achieving a homogeneous gas blanket.
- **Limited inlet points:** With only two gas inlets, the original configuration failed to ensure uniform argon coverage, especially noticeable in central and extreme edges of the welding surface, as confirmed by simulations.

Based on the initial experimental and simulation outcomes, modifications were necessary to optimize shielding performance. Specific design constraints were established: flow channel length had to remain constant, while diameter alterations and adjustments to inlet shapes were permitted within structural limits. Early ideas included incorporating flow-obstructing features to regulate gas distribution more precisely; however, these were subsequently abandoned due to design complexity which could lead to manufacture defects and marginal improvements.

The initial simulations provided clear guidance for improvements, notably the necessity to minimize sharp internal geometries, increase inlet points for more uniform gas distribution, and reconsider the utility of smaller internal tubing. These conclusions were supported by existing literature, which extensively documents the relationship between internal geometry and flow turbulence in welding gas distribution systems (CAMPBELL et al., 2013) and (SCHRICKER; BAUMANN; BERGMANN, 2021).

These insights defined the pathway toward subsequent design iterations, setting the foundation for targeted structural enhancements aimed at achieving homogeneous, laminar gas flow and effective oxidation control.

4.3 Iteration 2 - Enhanced Distribution

Building upon the initial simulation results and insights from existing research, several targeted modifications were systematically applied to enhance gas distribution efficiency in the gas supply structure. Each modification was individually implemented and evaluated via Computational Fluid Dynamics (CFD) simulations in ANSYS Fluent, thereby enabling precise identification of improvements or regressions in performance. The final designs of version 2 are presented in the appendix (Drawing: Mask 1 V2 and Drawing: Mask 2 V2).

Firstly, the number of gas inlets increased from two to four on each side of the shielding masks. This change aimed at promoting more uniform gas distribution across the welding surface. Initially, the new inlets for the first mask were planned to connect directly to the midpoint of the external tubing. However, contraints from integration in clamping fixture necessitated repositioning these inlets slightly away to the midpoint to avoid interference.

The structural design of the inlets underwent a significant geometric modification, transitioning from simple circular openings (initially 6.4 mm diameter) into trapezoidal profiles, achieved using SolidWorks' lofted cut tool. Specifically, the inlet profiles expanded from a circular shape to a rectangle measuring 25 mm by 4 mm. This trapezoidal geometry facilitates a gradual expansion, thereby improving the distribution and minimizing turbulence of the incoming argon gas, as supported by literature (CAMPBELL et al., 2013).

Another significant modification involved eliminating the smaller internal tubing and its connections, notably improving overall gas flow characteristics, particularly in the first mask. Additionally, the exit points from the internal tubing to the atmosphere were strategically repositioned further back to minimize premature gas escape, enhancing gas retention within the shielding structure and consequently improving overall effectiveness.

Rounded corners were introduced in all internal pathways to reduce abrupt changes in direction and mitigate turbulence. The theoretical justification for this modification aligns with established fluid dynamics principles, where smooth, rounded geometries are known to significantly decrease flow turbulence and improve laminar flow characteristics (MUNSON, 2010).

Furthermore, the outlet geometry was modified to a trapezoidal shape using SolidWorks' chamfer tool to incline the walls of the outlet openings. This geometric optimization was intended to reduce the gas flow to the atmosphere. The angle between the gas flow vector and the opening wall creates a vortex that helps to keep the gas contained above the welding surface. The interaction between a fluid jet and an inclined surface induces complex flow behavior marked by vortex formation, asymmetrical flow

structures, and shear layer instabilities, (MIRIKAR et al., 2024) and (ROY et al., 2002). Studies on pulse jet impingement reveal that vortices formed in the shear layer significantly enhance fluid mixing and entrainment capabilities, Figure 5. These insights underpin the hypothesis that utilizing inclined outlet geometries in gas shielding structures can improve gas retention near welding zones by generating stable vortical barriers, thus limiting dispersion into the atmosphere.

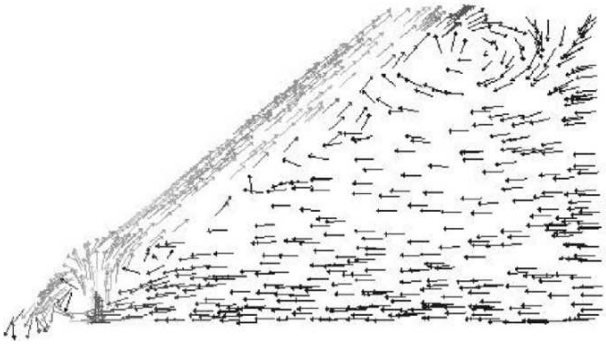

Figure 5 – Vortex generation in shear layer

Source: (ROY et al., 2002)

Following simulation-based validation of these design enhancements, the finalized second-iteration structures were prepared and sent for 3D printing, allowing subsequent physical testing and validation in practical welding scenarios.

4.4 Iteration 3 - Final Optimized Geometry

The third and final iteration focused on refining the enhancements identified during the second iteration, involving extensive simulations and experimental validations to optimize gas distribution and welding efficiency. After these rigorous analyses and validations, the optimized geometry was finalized and subsequently prepared for 3D printing. The final design of this iteration is presented in the appendix (Drawing: Mask 1 V3 and Drawing: Mask 2 V3).

Initially, a substantial redesign was explored by repositioning two gas inlets towards the center of the first mask and dividing the internal tubing into four disconnected segments. However, simulations indicated no significant improvements, prompting the abandonment of this concept. Figure 6 shows this design and Figure **??** the simulation of it.

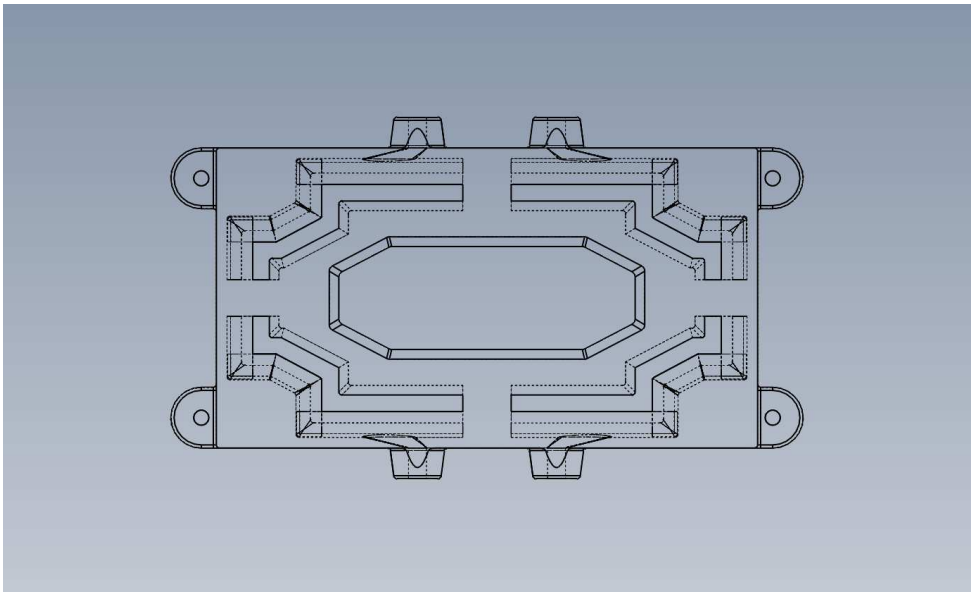

Figure 6 – Design for divided tubing mask

Source: Author

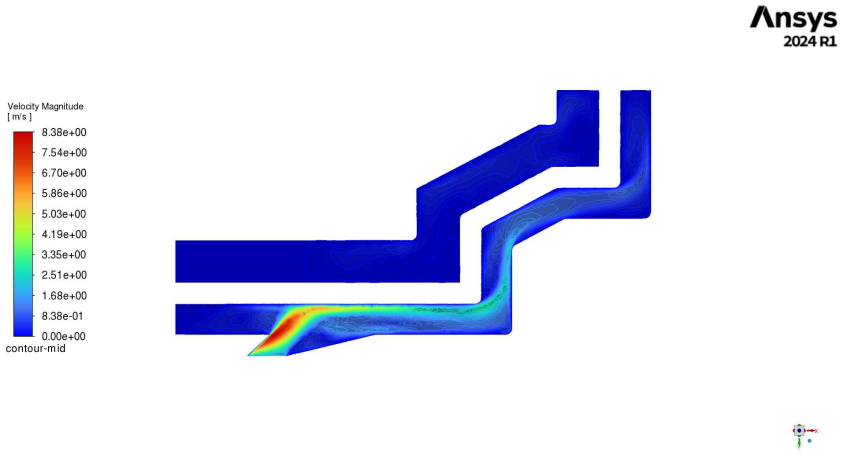

(a) Middle section view

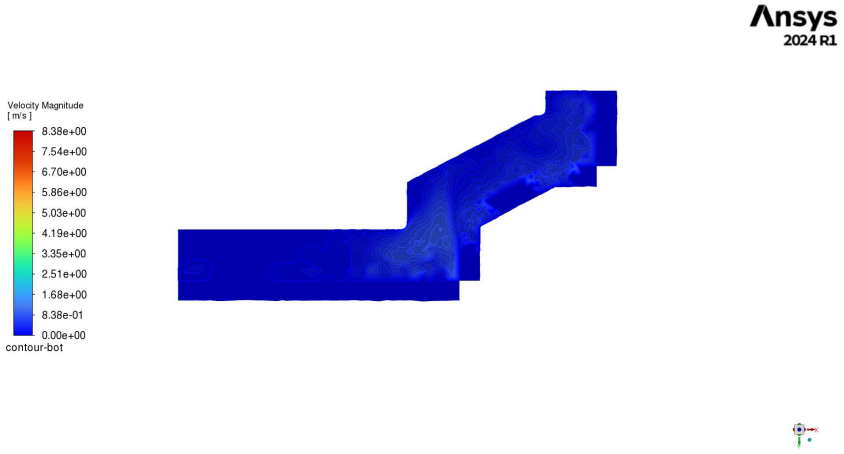

(b) Bottom section view

Figure 7 – Simulation for divided tubing mask

Source: Author

The middle-plane, Figure 7a, shows a localized high-velocity region (highlighted in red) at the inlet, indicating effective gas entry. However, despite this promising start, the bottom-plane, Figure 7b, reveals insufficient gas retention over processing zone, characterized by predominantly low-velocity regions. These simulations indicated that while repositioning the inlets and dividing the tubing could potentially increase localized gas velocity, it did not significantly enhance the overall distribution uniformity or coverage efficiency.

Several effective modifications emerged through detailed simulations and practical tests. Reducing the internal tubing diameter proved successful, as it increased gas velocity and improved coverage, consistent with fluid dynamics literature stating that smaller tubing diameters enhance gas velocity and distribution efficiency (CAMPBELL et al., 2013). Additionally, refining the gas outlet geometry by making it narrower and positioning it further back within the internal tubing significantly decreased premature gas escape,

thereby improving gas retention and overall coverage.

Modifications to the inlet structure included widening the opening and integrating a triangular diffuser. This geometric adjustment improved gas diffusion at entry, reducing turbulence and achieving a more uniform, laminar gas flow across the welding surface, aligning with the theory in (MUNSON, 2010).

Simulations also revealed substantial gas leakage at the curves of the internal tubing. Addressing this issue by blocking these exit points at the curves greatly minimized unintended gas loss, thus enhancing overall gas utilization efficiency, this change can be observed in Figure 8.

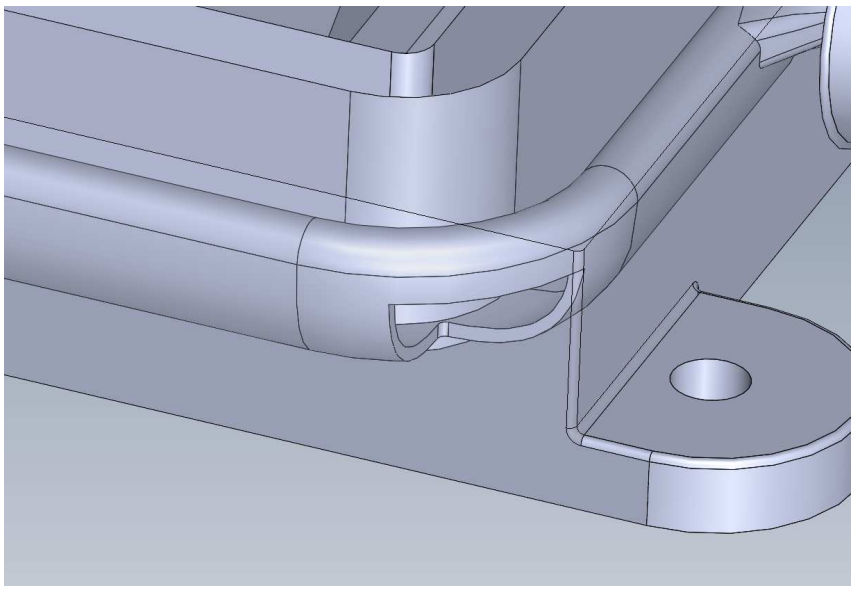

Figure 8 – Detail view of blocked curves exit points

Source: Author

Initially, triangular outlet geometries informed by existing literature were implemented, anticipating vortex formation at higher flow velocities. However, subsequent simulations and comparisons indicated that these triangular geometries were ineffective at the lower velocities used in this design, failing to generate vortices and inadvertently expanding the gas coverage area. Reverting to a simpler rectangular outlet geometry resulted in better targeted gas coverage and improved efficiency, aligning more effectively with simulation results.

4.5 Experimental Setup

Initially, the printed components were assembled into an existing welding fixture previously designed and constructed by another researcher. The clamping system consists

of a base plate and a clamping mask. Half shells are sandwiched between the two using predefined clamping force. A bevel is used along the welding paths for accessibility of the laser. The supply fixture developed for distributing the shielding gas is mounted on the clamping mask. This allows provision of gas from top side of the BPP. To provide shielding gas from the bottom side, grooves are created directly into the base plate. Placing the half plates over the grooves closes it off and enables reliable flooding with shielding gas. The mask and fixture are designed for both welding steps and allow the welding paths to overlap. Pictures of the welding assembly are confidential and can not be shown here, but figure 9 shows a diagram of the welding structure.

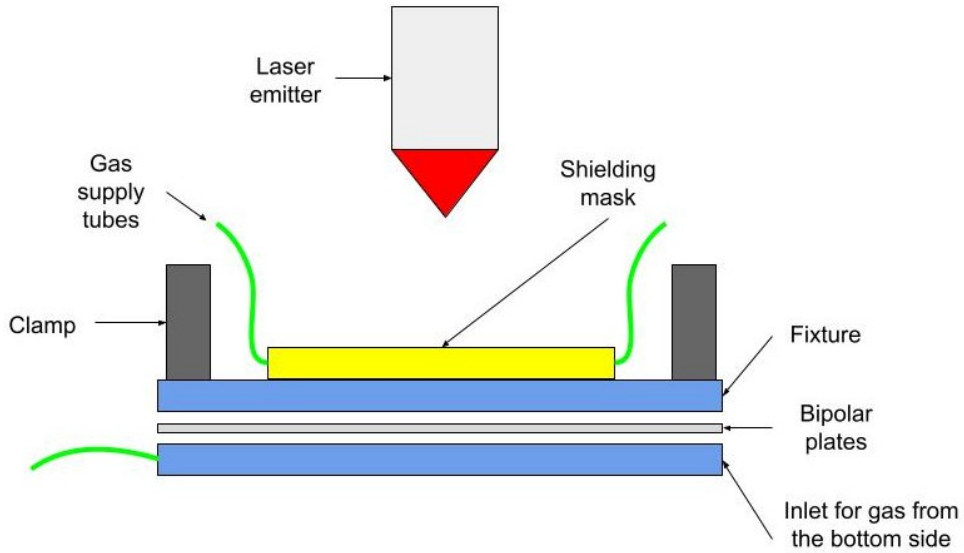

Figure 9 – Assembled welding structure

Source: Author

The experimental procedure involved conducting weld tests across a range of shielding gas flows, starting from 22 L/min and decrementing in steps of 2 L/min down to 10 L/min. Each gas flow setting was applied individually to both optimized mask versions. The original mask version was excluded from this specific experimentation phase, as did not show promising results from simulation. Laser process paramters were predefined and kept constant throughout the entire experiment.

Following the welding tests, each welded sample was examined using an optical microscope at a magnification of 250x. This optical analysis aimed to determine both the locations and characteristics of any oxidation observed on the samples, thereby allowing identification of the optimal gas flow. Subsequently, the most effective flow rate, identified as 12 L/min, was selected, and five additional plates were welded at this setting for both iterations to verify the reproducibility of the results.

To facilitate an in-depth understanding of the oxidation characteristics and welding performance, cross-sectional analysis was conducted. Sections of the plates representing both the poorest performing flow scenario (22 L/min) and the optimal condition (12 L/min) for each mask design were prepared. Additionally, a baseline reference sample welded without any gas shielding mask was included for comparison. All these sectioned samples were then submitted for metallographic examination, which involved capturing detailed cross-sectional images using Scanning Electron Microscopy (SEM). Furthermore, Energy Dispersive X-ray Spectroscopy (EDX) analysis was performed to evaluate the chemical composition of the cross-sections, providing insight into oxidation behavior and effectiveness of the shielding designs. The results and analysis of these investigations are presented and discussed in the subsequent chapter.

5 Analysis of results

This chapter presents the evaluation of the gas shielding system based on the results obtained from computational simulations and experimental welding tests. The analysis focuses on verifying whether the design iterations improved gas flow distribution and reduced oxidation on the weld surface. Simulation results are compared across all three mask iterations to assess flow uniformity and the presence of stagnation zones. Experimental outcomes are discussed in terms of oxidation patterns observed under optical microscopy, supported by cross-sectional analysis through Scanning Electron Microscopy (SEM) and Energy Dispersive X-ray Spectroscopy (EDX). These cross-sectional examinations are also used to assess the quality of the welds, providing additional insight into the structural effects of shielding performance. The objective is to determine the effectiveness of each design in meeting the defined requirements for gas shielding and weld integrity.

5.1 Computational Fluid Dynamics (CFD) Simulation Results

This section presents the results of the simulation-based evaluations performed on the three design iterations of the gas shielding masks. CFD simulation were done at fixed inlet velocity of 1.98 m/s, which corresponds to an experimental argon flow rate of 12 L/min, the optimal condition identified during experimental validation.

The objective of this simulation analysis is to investigate the evolution of internal flow behavior across iterations and to correlate these findings with experimental oxidation observations. Each design was simulated in cross-sectional and bottom views, highlighting the influence of geometric parameters such as internal tube curvature, outlet positioning, and inlet cross-sectional area on flow uniformity and reduction in stagnation/reduction in processing zones without shielding gas.

Figures 10 and 11 depict simulation results of argon gas flow within the baseline shielding gas structure for welding bipolar plates, obtained using ANSYS Fluent. The middle, Figures 10a and 11a, and bottom, Figures 10b and 11b, views of the masks reveal uneven gas distribution across the structure. In particular, gas velocity drops substantially as the flow moves away from the entry points, leading to poor coverage at central and edge areas of the weld surface. This displays issues in the baseline design: insufficient inlet points and internal sharp geometries cause inadequate and non-uniform argon coverage, thus failing to provide effective shielding.

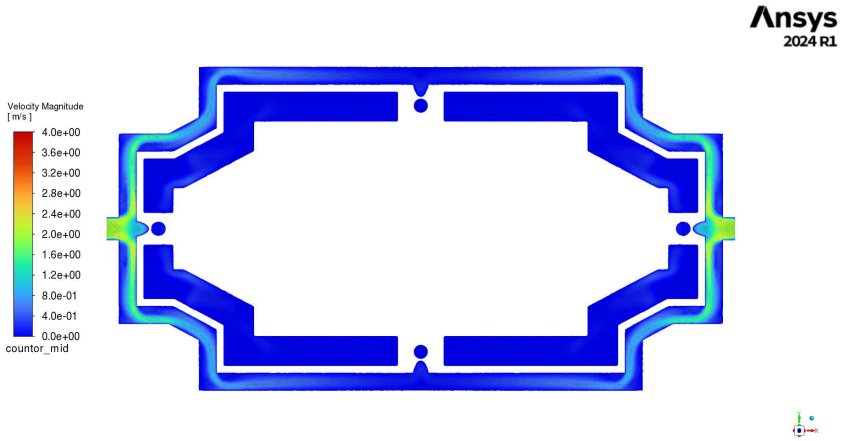

(a) Middle section view

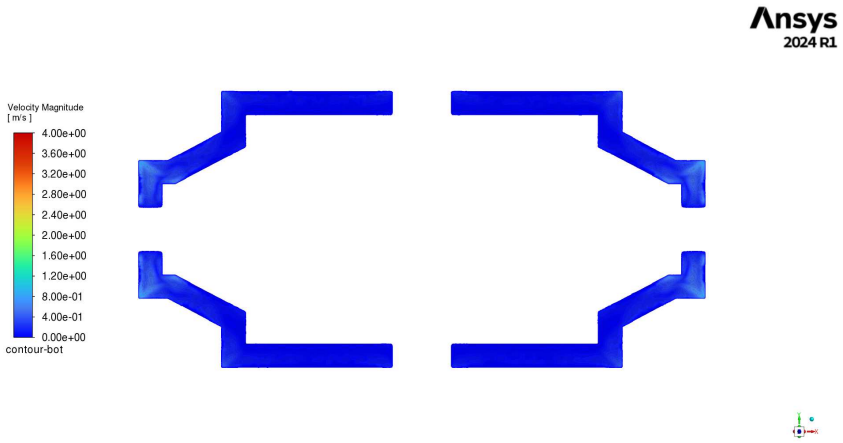

(b) Bottom section view

Figure 10 – Simulation for Mask 1 V1

Source: Author

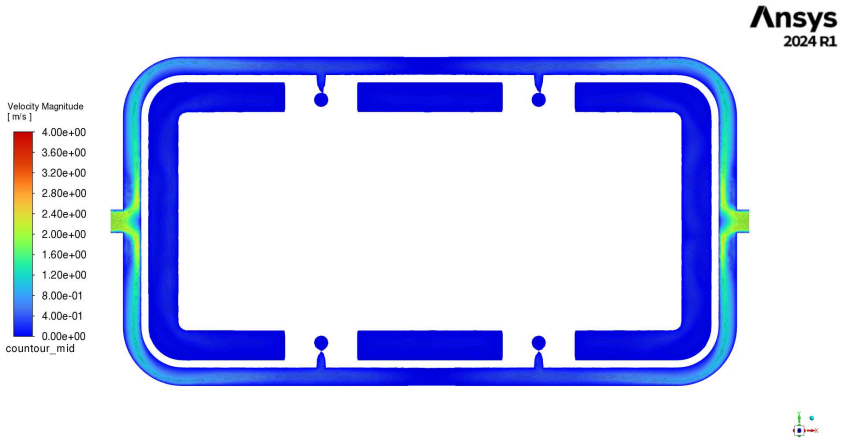

(a) Middle section view

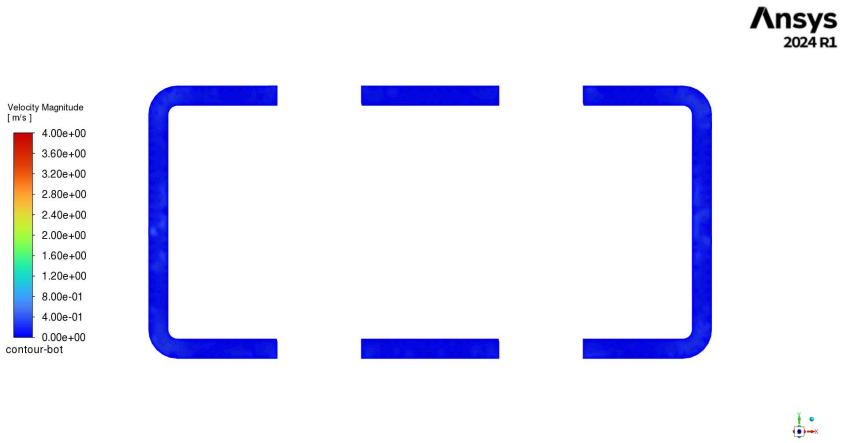

(b) Bottom section view

Figure 11 – Simulation for Mask 2 V1

Source: Author

The cross-section of flow channel, Figure 12, illustrates the behavior of the outlet design. The center bottom exit opening observed on the outer tubing promotes an easier escape point for the gas, decreasing the structure saturation. The shape of the opening, which resembles an inverted trapezoid, facilitates the spread of the gas to the atmosphere, resulting in a decrease in the consistent gas coverage over the welding surface; this behavior is consistent with the function of divergent diffusers in fluid systems, where a gradual area expansion is employed to convert kinetic energy into pressure energy and promote uniform flow dispersion (MUNSON, 2010).

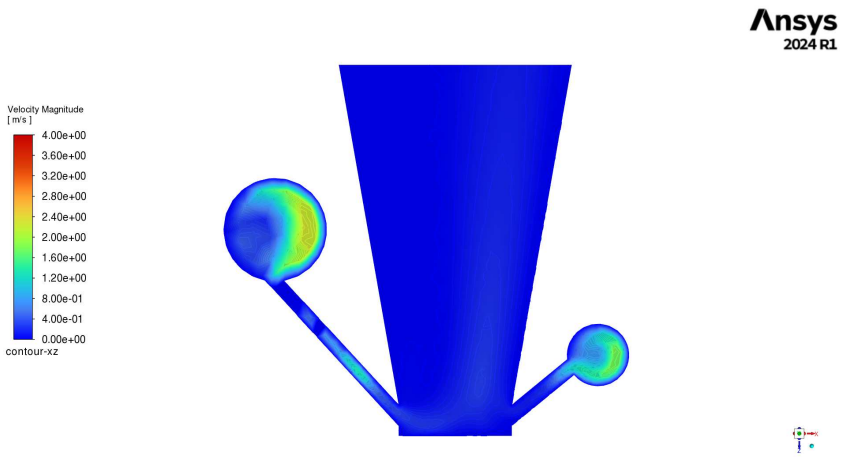

Figure 12 – Cross-section of flow channel from iteration 1

Source: Author

The second iteration's simulation results demonstrate notable improvements in argon gas distribution within the shielding structure, Figures 13 and 14. From the middle and bottom views, the enhanced inlet geometry, specifically the trapezoidal openings with gradual expansion from a 6.4 mm diameter circle to a 25x4 mm rectangle, shows significantly improved distribution. The new design effectively reduces stagnation and turbulent flow zones that were prominent in the first iteration.

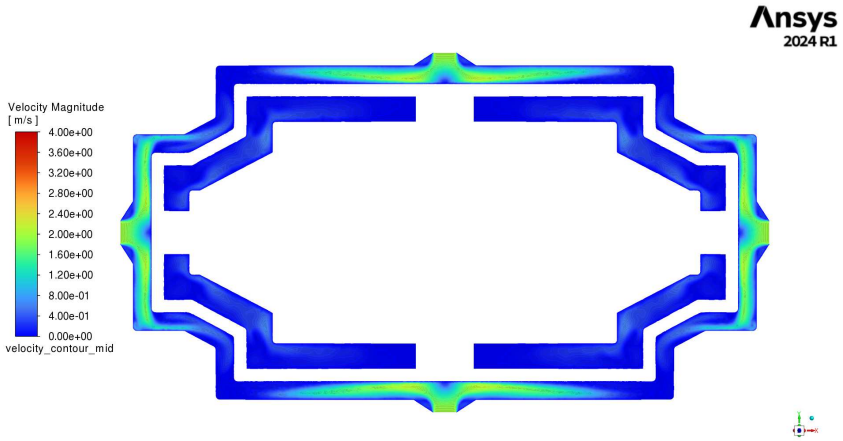

(a) Middle section view

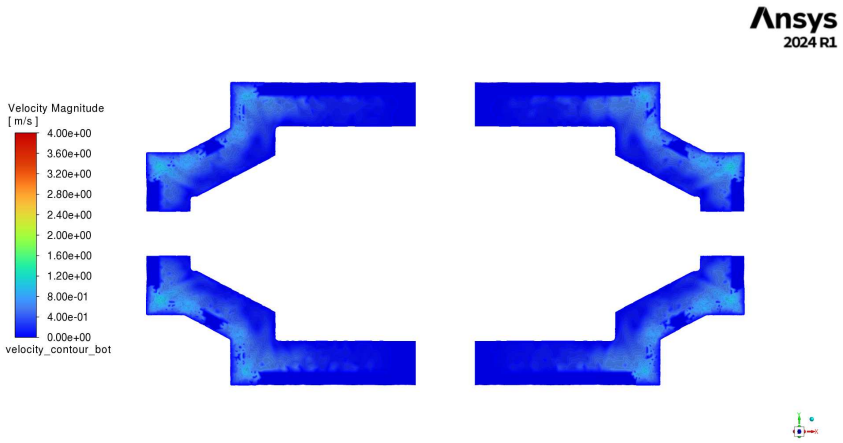

(b) Bottom section view

Figure 13 – Simulation for Mask 1 V2

Source: Author

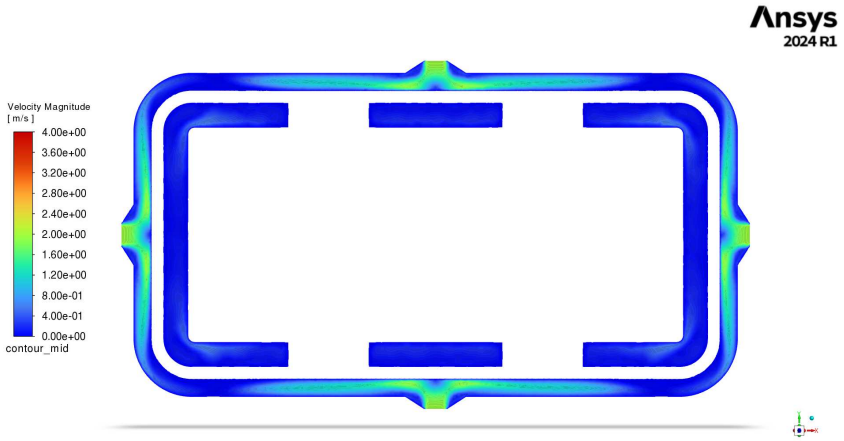

(a) Middle section view

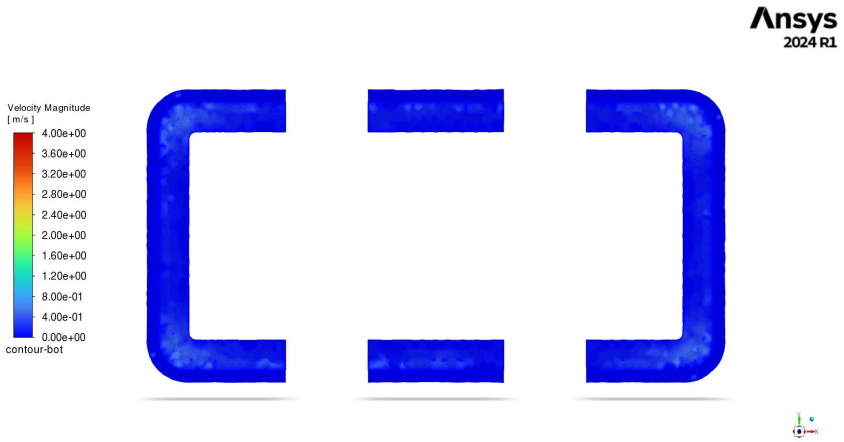

(b) Bottom section view

Figure 14 – Simulation for Mask 2 V2

Source: Author

The bottom view clearly indicates a more uniform and widespread gas distribution across the welding area. The additional inlets integrated into the design facilitate better flow uniformity, significantly reducing the previously observed areas of low velocity and poor gas coverage. Despite these improvements, some residual non-uniform gas distribution persist, particularly near the extremities and certain central areas, suggesting further refinements may be necessary.

Additionally, the removal of internal tubing and incorporation of rounded internal corners appear to have contributed substantially to a smoother gas flow, minimizing turbulence as indicated by the improved velocity uniformity. However, subtle variations in gas distribution still highlight the importance of further optimizing inlet and internal geometries to achieve consistently superior shielding performance across the entire weld surface.

The simulation result depicted in Figure 15a illustrate the cross-sceetion velocity contours for the second design iteration. In the second iteration, the outlet features a triangular geometry designed to exploit flow detachment and vortex formation as suggested by prior literature on inclined outlet surfaces. The aim was to induce shear layer instabilities and promote recirculation zones to contain gas near the weld surface. However, the results reveal that at the operating flow velocity of 1.98 m/s, this geometry does not generate any significant vortex structures. Instead, gas exits the system prematurely, dispersing across a wide area and failing to maintain a concentrated shielding layer near the weld region. The velocity magnitude remains low and uniformly distributed, with no localized high-velocity recirculation indicative of vortex behavior.

In contrast, the third iteration, Figure 15b, adopts a simplified rectangular outlet with a narrower and more recessed opening. The simulation clearly shows that the gas is more effectively retained within the structure, with increased velocity gradients localized near the outlet. The flow direction is more aligned along the surface plane, avoiding the radial spread observed in the previous design. As a result, the gas distribution becomes more targeted and laminar, reducing waste and ensuring more consistent shielding performance over the weld seam.

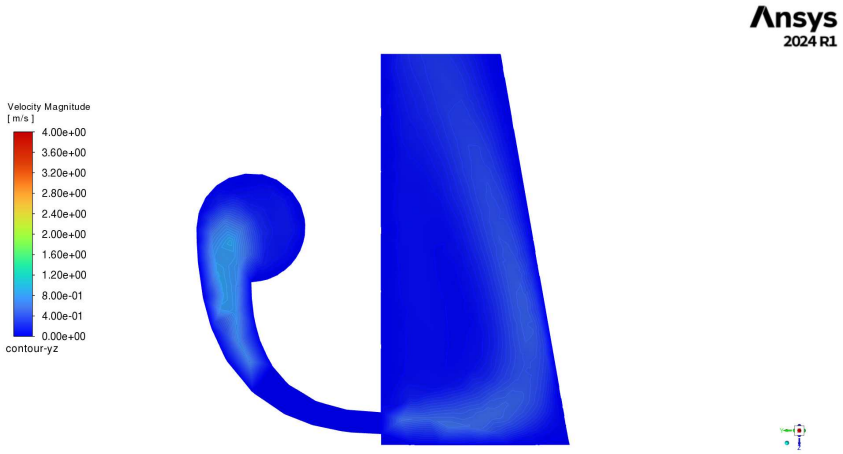

(a) Cross-section V2

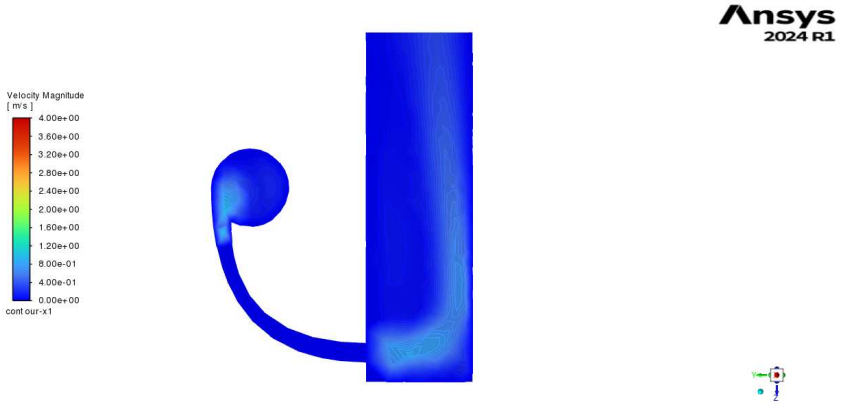

(b) Cross-section V3

Figure 15 – Cross-section comparison of the outlet designs of iterations 2 and 3

Source: Author

The middle and bottom results for the simulations of the third iteration can be observed in Figure 16 for the first mask and in Figure 17 for the second mask. The simulation results from Iteration 3 clearly illustrate the improvements in gas distribution achieved through the final geometric optimization. From the middle-plane views, it is evident that gas enters uniformly from the redesigned inlets, diffusing effectively due to the widened inlet and triangular diffuser, resulting in increased velocity along the internal channels. Bottom-plane images further confirm these enhancements, showing a more consistent and uniform gas distribution across the entire welding surface. The blocking of unnecessary gas leakages at curves and strategic narrowing of the outlet region effectively minimized turbulence and improved laminar flow characteristics. Consequently, the optimized geometry enhanced overall gas coverage and efficiency.

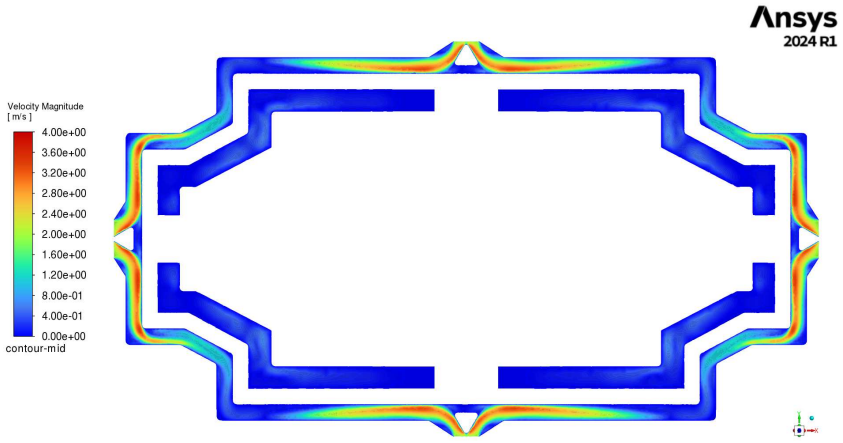

(a) Middle section view

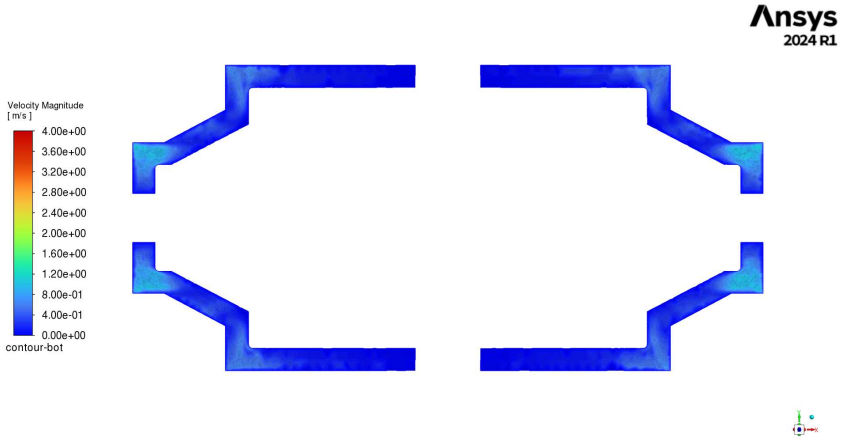

(b) Bottom section view

Figure 16 – Simulation for Mask 1 V3

Source: Author

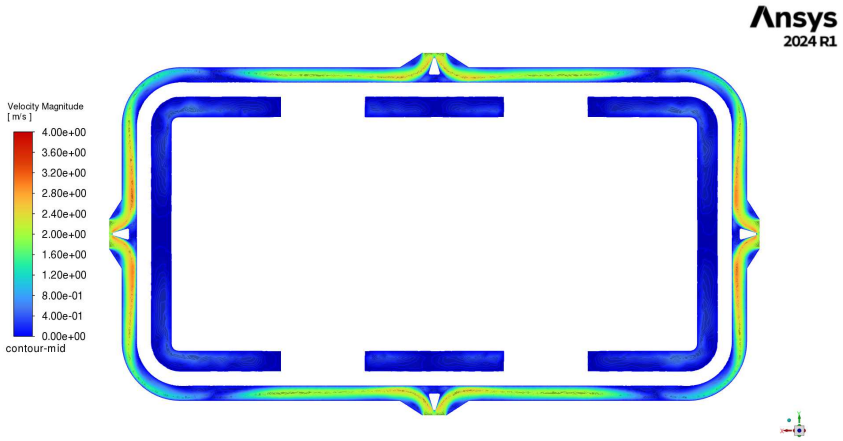

(a) Middle section view

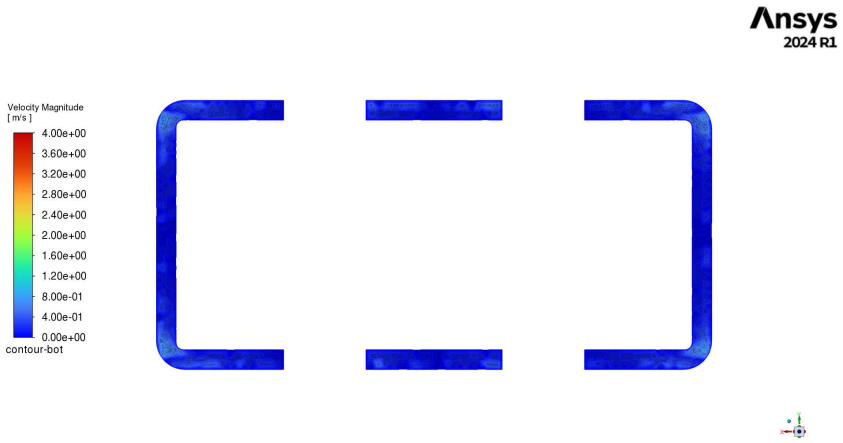

(b) Bottom section view

Figure 17 – Simulation for Mask 2 V3

Source: Author

A summary of the simulation results across all three iterations is presented in table 2. This table highlights the key differences in inlet and outlet geometries, internal flow characteristics, and overall gas coverage efficiency. The progression from the first to the third iteration demonstrates a clear trend towards improved shielding performance, with each design iteration addressing specific shortcomings identified in previous simulations. Table 3 provides a visual comparison of the middle and side views for each iteration, illustrating the evolution of gas flow characteristics and coverage across the designs.

Table 2 – Comparison of Simulation Results Across Iterations

Aspect	**Iteration 1 (V1)**	**Iteration 2 (V2)**	**Iteration 3 (V3)**
Inlet Geometry	2 circular inlets	4 trapezoidal inlets	4 widened trapezoidal inlets with central diffuser
Internal Geometry	Sharp curves, small tubes	Rounded curves, removed small tubes	Thinner tubes, blocked curve leak paths
Outlet Geometry	Inverted trapezoid	Triangular outlet	Narrow rectangular outlet
Middle View Result	Uneven flow, central stagnation	Improved coverage, still inconsistent edges	Higher-velocity flow
Bottom View Result	Poor weld coverage	Improved distribution	Near-complete coverage
Cross-section Result	Gas escapes quickly, no saturation	Broad dispersion, limited containment	Similar gas retention and directed flow
Flow Quality	Turbulent, ineffective	Improved, partially laminar	Better distributed
Overall Coverage	Incomplete and inefficient	Better, but not optimal	Best coverage observed

Table 3 – Comparison of Simulation Results for All Three Iterations: Middle and Side Views

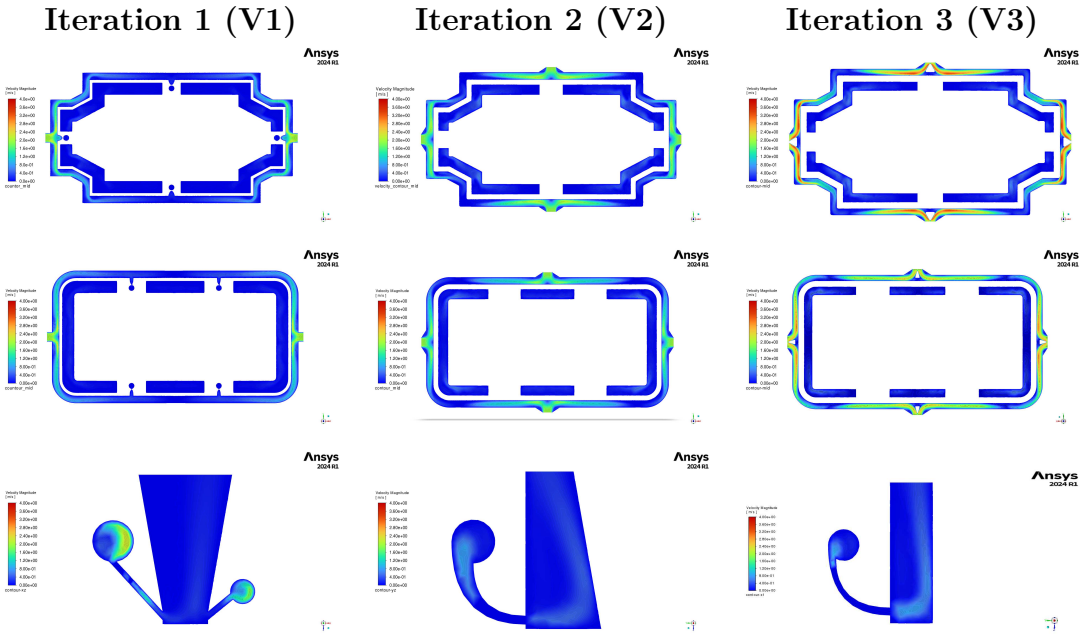

5.2 Optical Microscopy Analysis

To evaluate the effectiveness of the gas shielding designs in minimizing oxidation during laser welding, each welded sample was subjected to a detailed surface inspection using optical microscopy. This analysis aimed to identify oxidation patterns along the weld seam, assess their severity, and correlate these observations with the gas flow characteristics predicted by the simulations.

All welded plates were examined at a magnification of 250x, which enabled the detection of surface-level oxidation features such as discoloration, oxide film formation, and weld spatter. This method provided qualitative spatial data on oxidation distribution, particularly distinguishing between well-shielded and poorly protected regions. The optical analysis was applied to all the samples welded with each design iteration (V2 and V3) across a range of gas flow rates, from 22 L/min down to 10 L/min. Table 4 summarizes the experiments.

Table 4 – Summary of Experiment Parameters

Experiment	**Mask iteration**	**Gas Volume Flow Rate (L/min)**
1	2	22
2	2	22
3	2	22
4	2	20
5	2	18
6	2	16
7	2	14
8	2	12
9	3	10
10	3	22
11	3	20
12	3	18
13	3	16
14	3	14
15	3	12
16	3	10

The principal aim of this analysis was to ascertain the optimal flow conditions for each mask iteration and to corroborate the uniformity of oxidation reduction across multiple welds. Figure 18 presents a simplified schematic of the weld path, indicating the precise locations from which measurements were acquired. Specifically, point 1 corresponds to the source of both images in Figure 19, while point 2 denotes the location for the image in Figure 20. Point 3 indicates the origin of the image in Figure 21. Points 4 and 5 represent the locations from which the images for Tables 5 and 6 were obtained, with point 4 pertaining to Mask 1 and point 5 to Mask 2. Finally, points 6 and 7 signify the positions

where cross-sectional measurements were performed, with point 6 for Mask 1 and point 7 for Mask 2, resulting in a total of 10 cross-sectional measurements analyzed in Section 5.3.

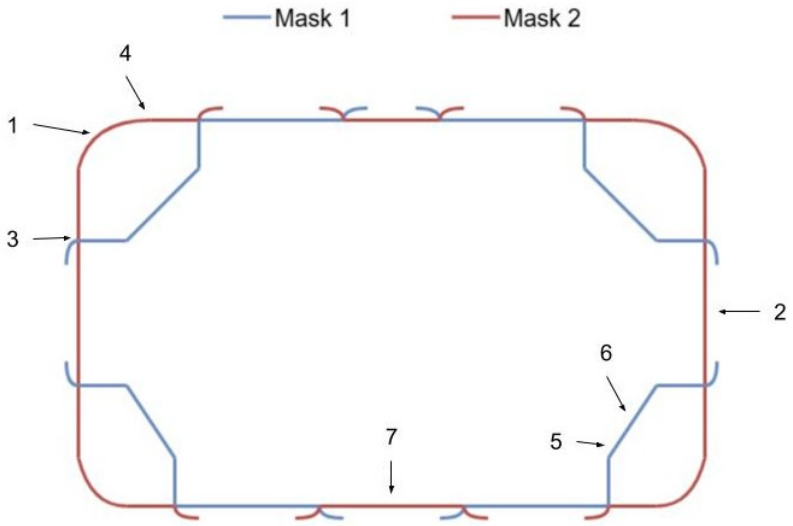

Figure 18 – Weld path sketch

Source: Author

For iteration 2, oxidation was widespread at higher flow rates (22 to 18 L/min), particularly affecting the top and right-side weld paths, see Figure 18. These areas consistently exhibited poor gas retention, with oxidation initiating early along the weld seam, especially in curved regions where flow stagnation was expected. In experiments 8 and 9 (12 and 10 L/min, respectively), a notable improvement was observed. The left-side curved area, previously oxidated, showed significant reduction in surface oxidation, Figure 19, indicating better flow containment under reduced flow conditions. This trend highlights a counterintuitive but critical result: lower flow rates in iteration 2 improved shielding performance by reducing turbulence and enhancing gas retention. Among all tests with iteration 2, Experiment 9 (10 L/min) produced the best result, with only minor oxidation points remaining on the left and some more prominent oxidation on the right, Figure 20.

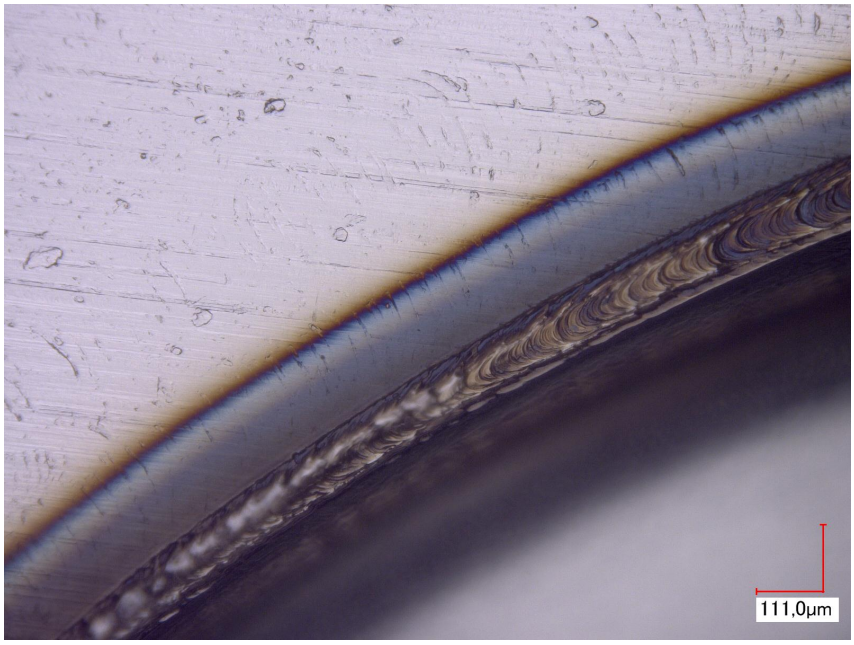

(a) iteration 2 with 22 L/min

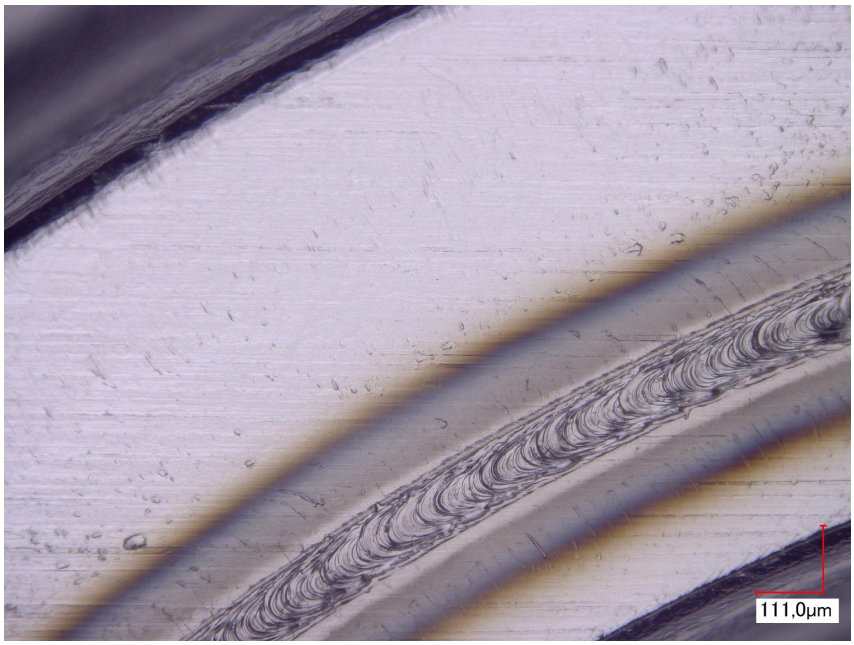

(b) iteration 2 with 10 L/min

Figure 19 – Comparison top left view of the weld path for iteration 2 with 22 L/min and 10 L/min

Source: Author

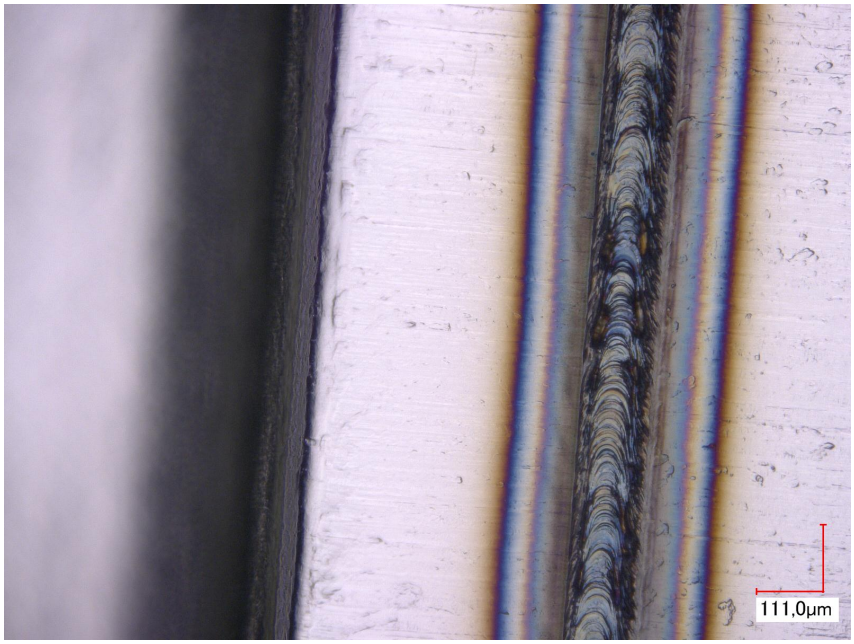

Figure 20 – Right view of the weld path for iteration 2 with 10 L/min

Source: Author

In iteration 3, substantial design improvements led to a noticeable decrease in oxidation across all flow conditions, particularly at 12 and 14 L/min. However, while oxidation was significantly reduced, it was not eliminated. Visual oxidation remained at the beginning of several weld paths, typically near the edges of the outlet openings, Figure 21. This behavior correlates with simulation results, which showed weaker gas coverage at these outlet-edge regions, there is no visible oxidation on the points were the weld paths overlap. Therefore, while iteration 3 achieved superior overall performance, the design still exhibits localized weaknesses, and cannot be considered optimal.

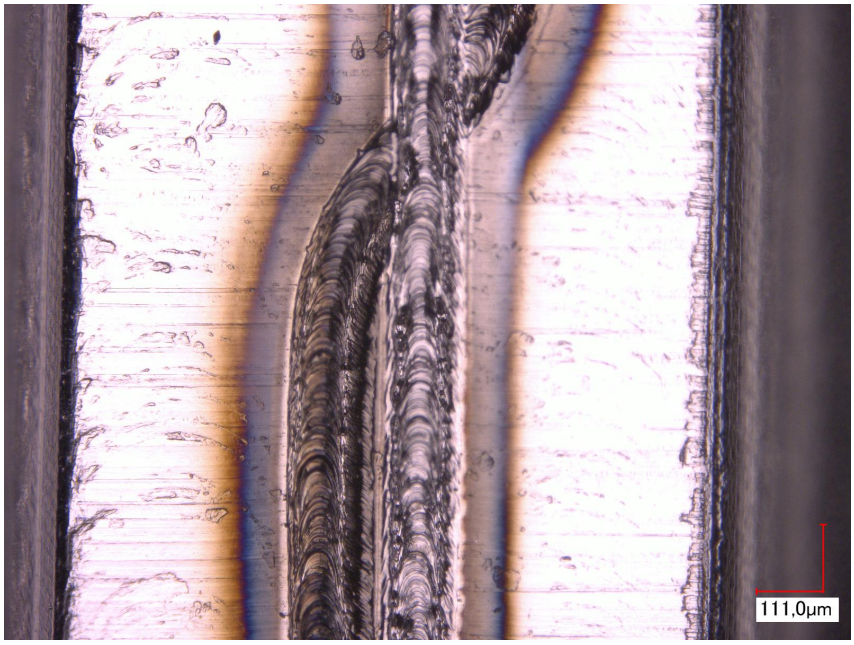

Figure 21 – Top left view of the weld path for iteration 3 with 12 L/min

Source: Author

Another relevant observation in iteration 3 is the consistent difference in oxidation between top and bottom, and left and right segments of the weld, despite the geometric symmetry of the shielding structure. This suggests the presence of external influences beyond the mask geometry itself, which are further discussed in the final conclusions.

Importantly, iteration 3 performed best at 12 L/min, where oxidation was least severe and mostly restricted to isolated surface-level spots. At 10 L/min, oxidation increased slightly, showing that there is a lower limit to effective gas shielding in this design. This contrasts with iteration 2, where 10 L/min yielded the best result. Still, the best result in iteration 2 (10 L/min) remains inferior to the worst result in iteration 3 at 22 L/min, underscoring the effectiveness of the final geometric iteration.

In summary, the optical analysis confirms that iteration 3 substantially improves shielding efficiency, particularly at moderate flow rates (12 - 14 L/min), but also reveals that gas coverage remains imperfect at the outlet periphery and is sensitive to asymmetries in flow supply or boundary conditions. These insights are critical for refining future designs.

Figure 22 exhibits the weld seam on the under side of the welded plates. This result is the same for all the welded plates for both iterations. On a surface level, the weld seam appears consistent, with no visible oxidation, discolouration or defects, which was expected because the bottom of the plate is not open to the atmosphere like the top is. However, it is still important to verify the internal structure of the weld with cross-sectional analysis.

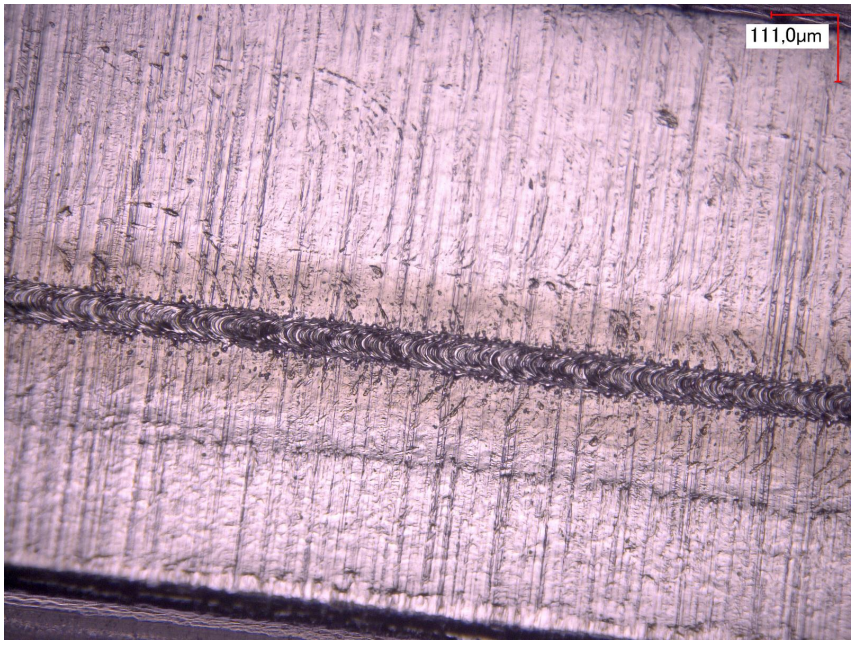

Figure 22 – Weld seam on the under side of the welded plates

Source: Author

Tables 5 and 6 display the superficial oxidation for each mask and each experiment, table 5 for iteration 2 and table 6 for iteration 3. Here it is easier to compare the different iterations and flow rates. For the first iteration, it is noticeable that that there is no significant improvement for the second mask for the specific point chosen for the analysis, all of the samples are oxidated. For the third iteration, in the first mask, altough there is some discoloration in experiments with 18 and 16 L/m, there is no visible oxidation, and for the second mask, experiments with 14 and 12 L/m also show no visible oxidation in a spot that, if compared to all the other experiments, oxidation is present. From these results, iteration 3 with 12 L/m was chosen as the best configuration, and further measurements were performed with cross-sectional analysis to verify this claim.

Table 5 – Optical Microscopy Results - iteration 2

Flow Rate	**Images**	
22 L/min	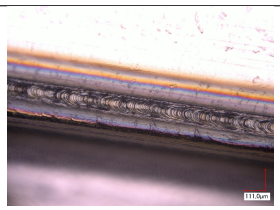 (a) Mask 1	 (b) Mask 2
20 L/min	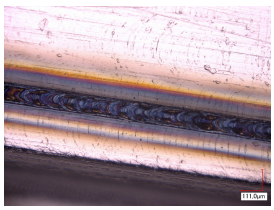 (c) Mask 1	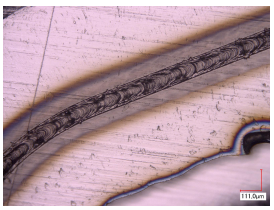 (d) Mask 2
18 L/min	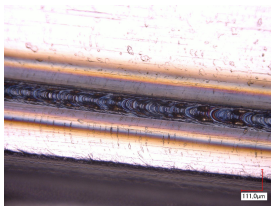 (e) Mask 1	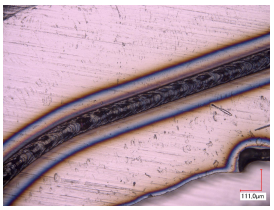 (f) Mask 2
16 L/min	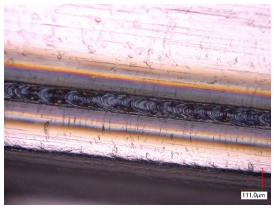 (g) Mask 1	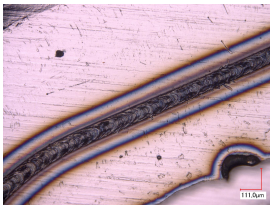 (h) Mask 2
14 L/min	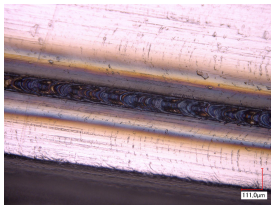 (i) Mask 1	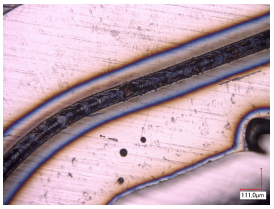 (j) Mask 2
12 L/min	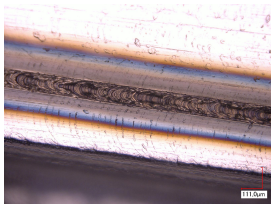 (k) Mask 1	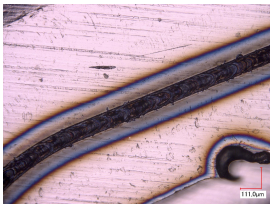 (l) Mask 2
10 L/min	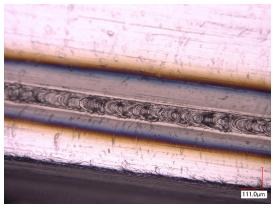 (m) Mask 1	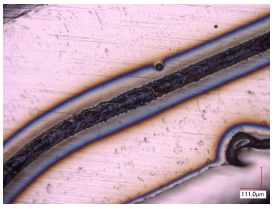 (n) Mask 2

Table 6 – Optical Microscopy Results - iteration 3

Flow Rate	**Images**	
22 L/min	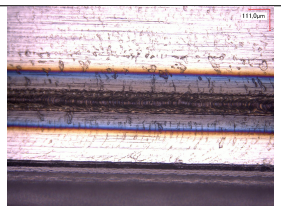	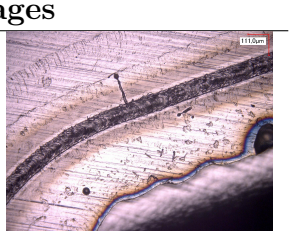
	(a) Mask 1	(b) Mask 2
20 L/min	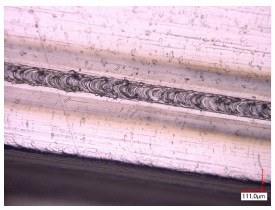	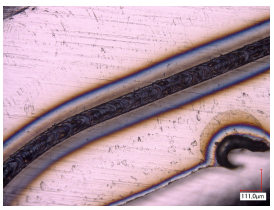
	(c) Mask 1	(d) Mask 2
18 L/min	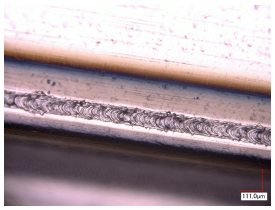	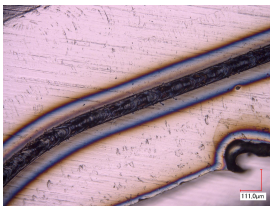
	(e) Mask 1	(f) Mask 2
16 L/min	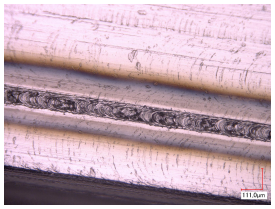	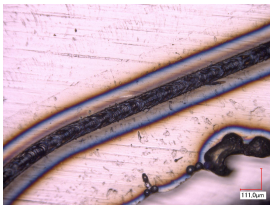
	(g) Mask 1	(h) Mask 2
14 L/min	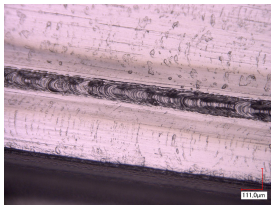	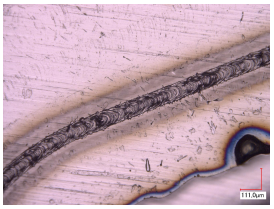
	(i) Mask 1	(j) Mask 2
12 L/min	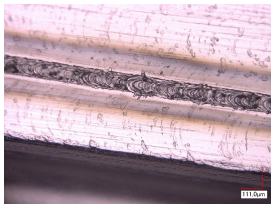	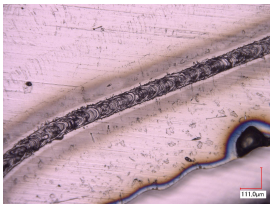
	(k) Mask 1	(l) Mask 2
10 L/min	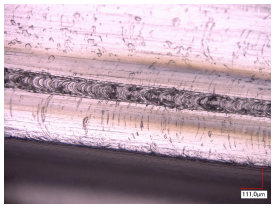	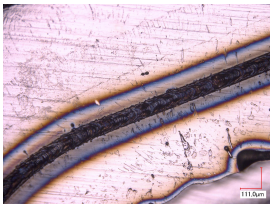
	(m) Mask 1	(n) Mask 2

The optical microscopy analysis across both mask iterations and flow conditions revealed progressive improvements in oxidation control, with results that align closely with simulation predictions. However, the analysis also confirms that no configuration achieved perfect surface protection, and certain geometric and flow-related limitations remain.

5.3 Cross-Sectional Analysis

To complement the surface-level observations obtained through optical microscopy and provide deeper insight into the nature and extent of oxidation within the welded joints, selected samples were subjected to cross-sectional analysis using Scanning Electron Microscopy (SEM) and Energy Dispersive X-ray Spectroscopy (EDX).

This analysis focused on representative samples from each mask iteration, chosen to reflect both the worst and best welding conditions observed during the shielding gas flow experiments. Specifically, cross-sections were prepared from welds produced at 22 L/min and 12 L/min for iteration 2, and at 22 L/min and 12 L/min for iteration 3, altough, for iteration 2 10 L/m had the best results, it was decided that an analysis of 12 L/m would be better as a comparison between both iterations. An additional reference sample, welded without any gas shielding structure, was also included to establish a baseline for oxidation severity.

SEM imaging was used to examine the microstructural integrity of the welds and to identify the depth and morphology of oxide layers within the weld seam and adjacent heat-affected zones. EDX analysis helped give a closer look at the grain distribution in the weld seam.

This combined method enables high-resolution visualization of oxidation penetration and offers a compositional profile that supports the identification of localized shielding failures.

For Mask 1 iteration 2 at 22 L/min, Figure 23, the SEM cross-section (Figure 23a) reveals a heterogeneous grain structure within the fusion zone, characterized by inconsistent grain size and shape. Clear linear discontinuities are visible at the edges of the weld, but there is not much porosity. The corresponding EDX oxygen map (Figure 23b) shows that oxygen is not uniformly distributed, but is instead concentrated along these linear paths and at the boundaries between grains, with concentrations ranging from 0.7% to 3.5%. This indicates that oxidation occurred preferentially at these microstructural interfaces.

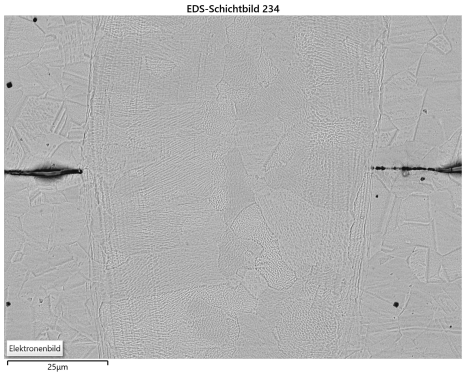

(a) Cross-sectional SEM

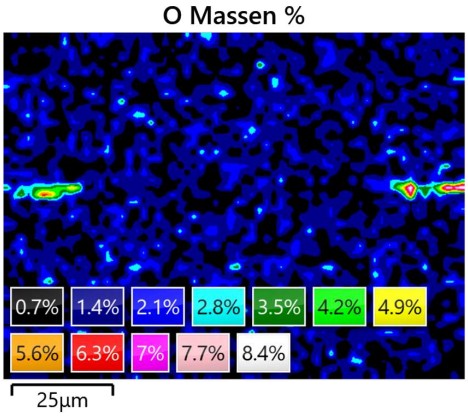

(b) EDX Oxygen Map

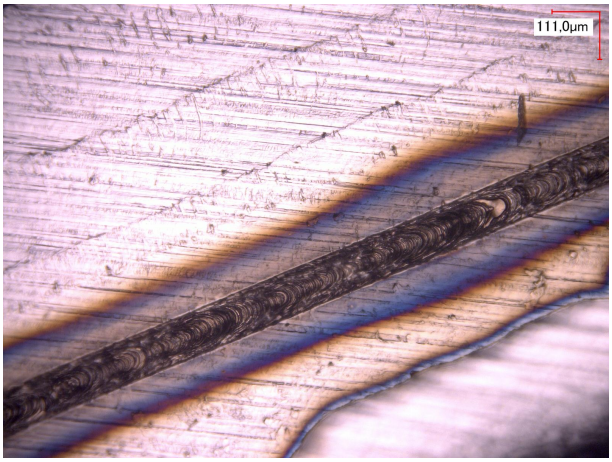

(c) Optical surface image

Figure 23 – SEM, EDX, and surface microscopy for (Mask 1, V2, 22 L/min)

Source: Author

In Mask 2 iteration 2 under the same condition, Figure 24, the weld's microstructure (Figure 24a) is similarly heterogeneous, characterized by an inconsistent grain size and shape. The inner structure of the weld is primarily composed of equiaxed grains, and the grain boundaries are clearly visible throughout the fusion zone. This sample also exhibits distinct linear discontinuities, which are most prominent at the edges of the weld. Some porosity is present within the microstructure, and the corresponding EDX map (Figure 24b) indicates that these pores are regions of high oxygen concentration.

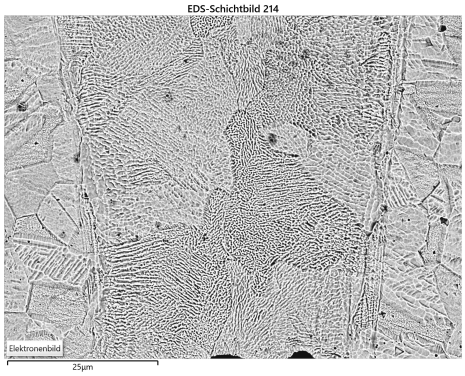

(a) Cross-sectional SEM

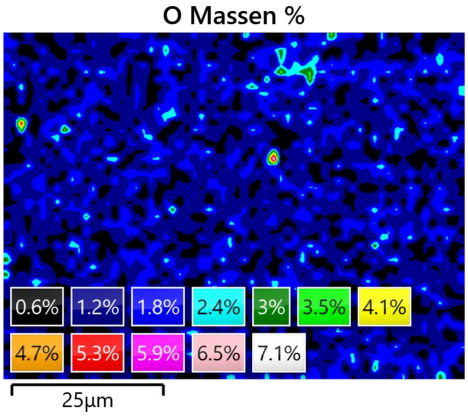

(b) EDX Oxygen Map

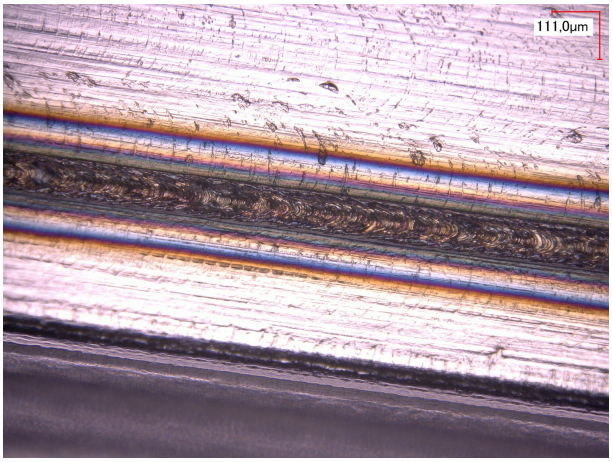

(c) Optical surface image

Figure 24 – SEM, EDX, and surface microscopy for (Mask 2, V2, 22 L/min)

Source: Author

At the reduced flow rate of 12 L/min for Mask 1, Figure 25, the weld microstructure is significantly compromised. While the structure (Figure 25a) is still composed of equiaxed grains and contains fewer linear discontinuities than the samples at higher flow rates, its integrity is poor. The most notable features are the large, dark grey patches of intragranular oxidation, which are not confined to grain boundaries. The corresponding EDX map (Figure 25b) confirms that these dark patches are the primary locations of severe oxygen concentration, with levels measured as high as 31%. Some porosity is also visible. Critically, these oxidized regions extend beyond the weld pool itself, indicating that the heat-affected zone was also severely contaminated.

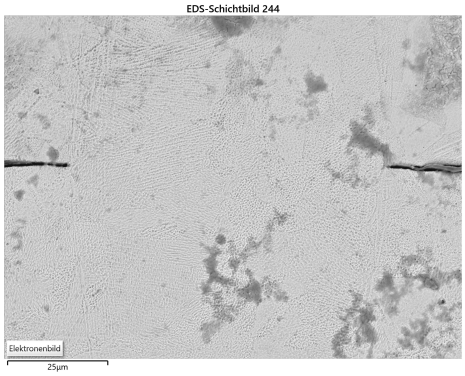

(a) Cross-sectional SEM

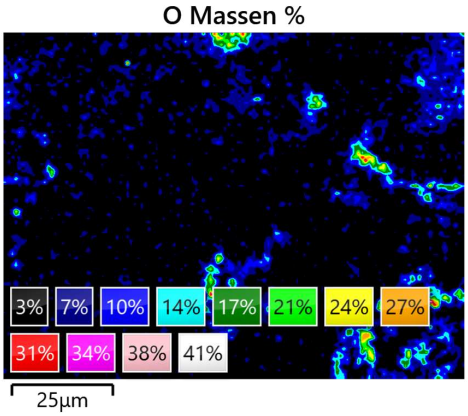

(b) EDX Oxygen Map

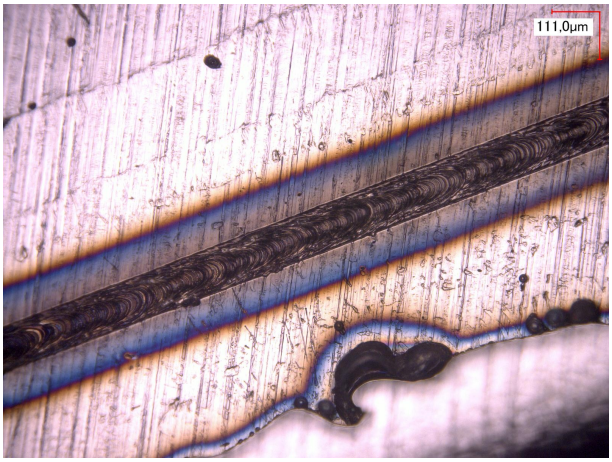

(c) Optical surface image

Figure 25 – SEM, EDX, and surface microscopy for (Mask 1, V2, 12 L/min)

Source: Author

In contrast, Mask 2 at 12 L/min, Figure 26, exhibits a substantially more consolidated weld profile. The microstructure (Figure 26a) is predominantly composed of equiaxed grains, and there is less visual contrast between the grain structure within the weld pool and the base material. While some smaller, dark grey patches and visible pores are present, prominent linear discontinuities are not easily identifiable. The EDX analysis (Figure 26b) confirms that these smaller grey patches correspond to areas of high oxygen concentration. Similar to the previous sample, some of these oxidized regions appear to extend beyond the weld pool into the heat-affected zone.

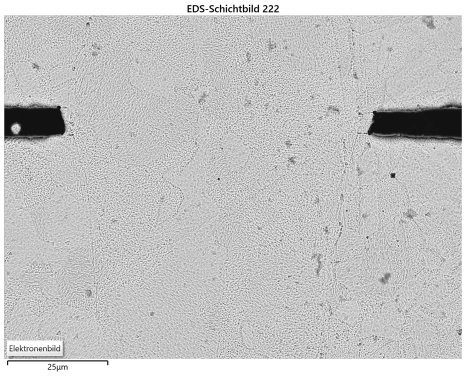

(a) Cross-sectional SEM

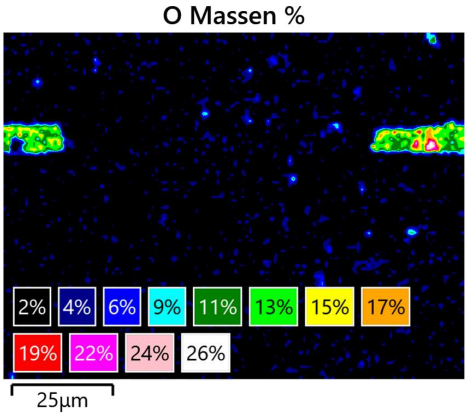

(b) EDX Oxygen Map

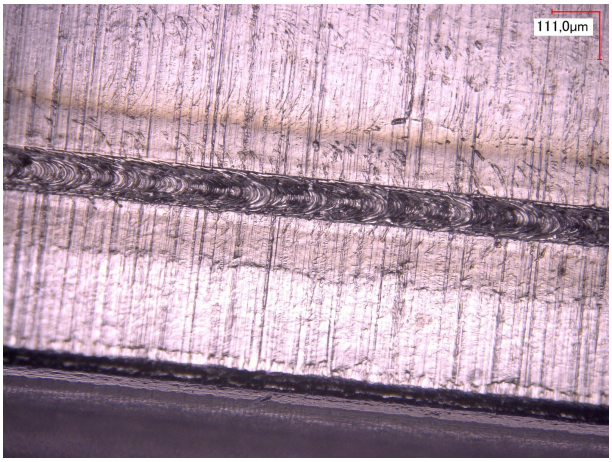

(c) Optical surface image

Figure 26 – SEM, EDX, and surface microscopy for (Mask 2, V2, 12 L/min)

Source: Author

For Mask 1 of Version 3 at 22 L/min, Figure 27, the cross-section shows a finer and more complex grain structure. The SEM image (Figure 27a) reveals a mix of both columnar grains and equiaxed grains of varying sizes. While prominent linear discontinuities are not identifiable, some clear pores are visible within the weld fusion zone. The corresponding EDX analysis (Figure 27b) confirms that these pores are areas of concentrated oxygen. Additionally, some very small grey patches, which present high oxygen concentration according to the EDX, can be observed in the material just outside the weld pool.

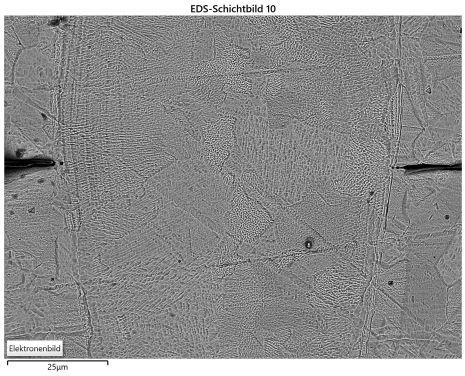

(a) Cross-sectional SEM

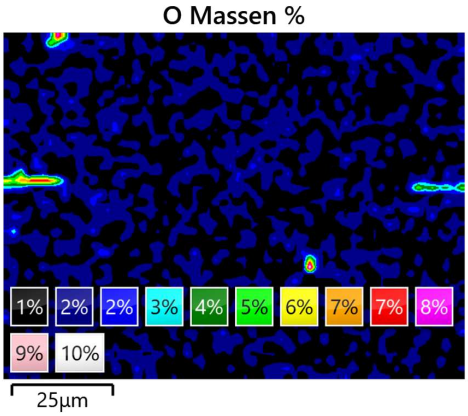

(b) EDX Oxygen Map

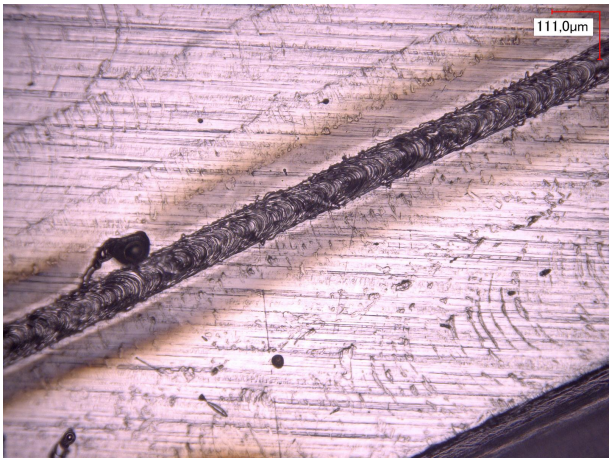

(c) Optical surface image

Figure 27 – SEM, EDX, and surface microscopy for (Mask 1, V3, 22 L/min)

Source: Author

For Mask 2 of Version 3 at 22 L/min, Figure 28, the weld exhibits a highly uniform and well-integrated microstructure. A key feature shown in the SEM image (Figure 28a) is the seamless transition between the weld pool and the base material, with no clearly defined boundary line. The grain structure is a mix of columnar and equiaxed grains, with some of the larger equiaxed grains showing a distinct triangular shape. The weld is largely free of defects, with minimal porosity and no identifiable linear discontinuities. A few very small, grey patches are visible, and they appear to follow the grain structure, which could signify intergranular oxidation. The EDX map (Figure 28b) indicates that these grey patches, along with the few visible pores, are the locations of higher oxygen concentration.

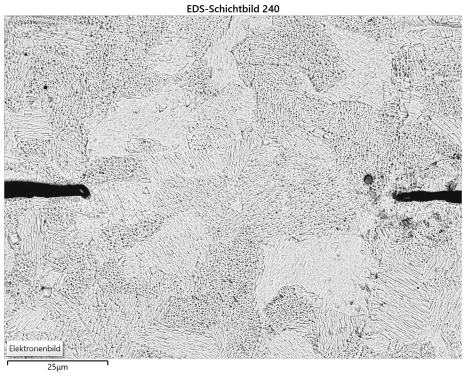

(a) Cross-sectional SEM

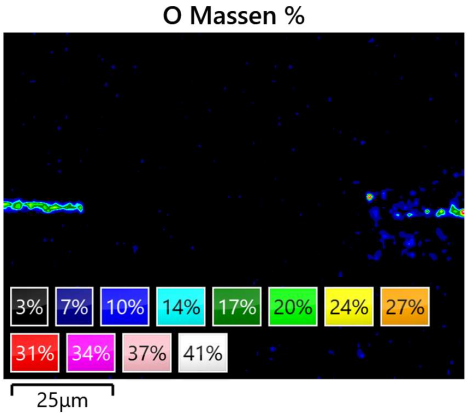

(b) EDX Oxygen Map

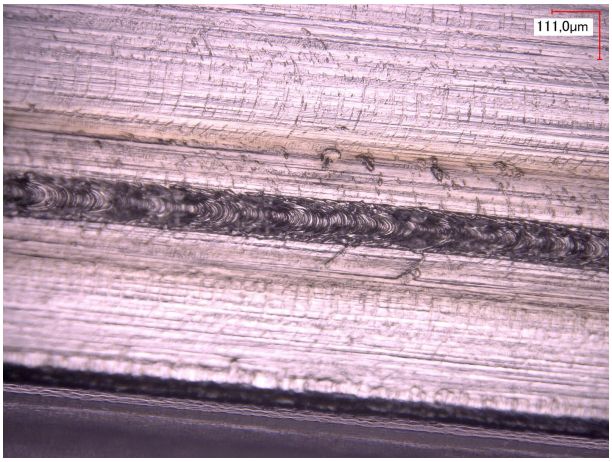

(c) Optical surface image

Figure 28 – SEM, EDX, and surface microscopy for (Mask 2, V3, 22 L/min)

Source: Author

For Mask 1 of Version 3 at 12 L/min, Figure 29, the SEM image (Figure 29a) displays a microstructure that is predominantly equiaxed, though the grains vary significantly in size, appearing in distinct patches of both small and large grains without a defined shape. There is no clear boundary between the structure inside and outside of the weld pool. The image also contains numerous straight lines; however, it is uncertain if these are features from the weld or artifacts from the sample preparation process. A high concentration of pores and many small, grey patches are visible throughout the structure. The EDX map (Figure 29b) confirms that these pores and grey patches are areas with a high concentration of oxygen.

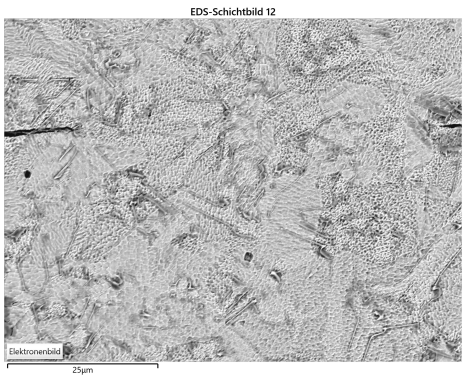

(a) Cross-sectional SEM

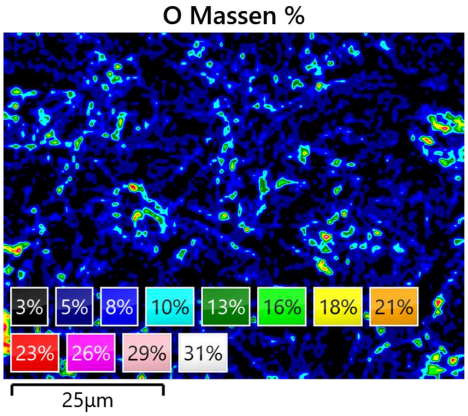

(b) EDX Oxygen Map

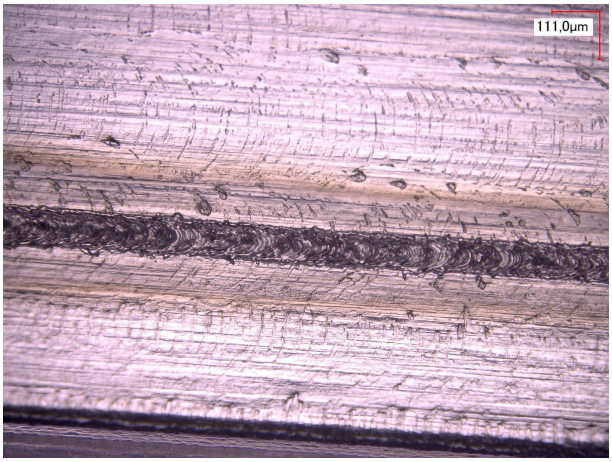

(c) Optical surface image

Figure 29 – SEM, EDX, and surface microscopy for (Mask 1, V3, 12 L/min)

Source: Author

Mask 2 of Version 3 at 12 L/min, Figure 30, represents the most homogeneous and structurally sound weld profile achieved. In the SEM image (Figure 30a), the boundaries of the weld pool are clearly defined. The grain structure is a mix of columnar and equiaxed grains which vary in size. The weld is remarkably free of defects; no linear discontinuities are identifiable, and only three very small, darker grey patches are visible. Some porosity is present, and the EDX map (Figure 30b) indicates that these pores are the primary locations of higher oxygen concentration.

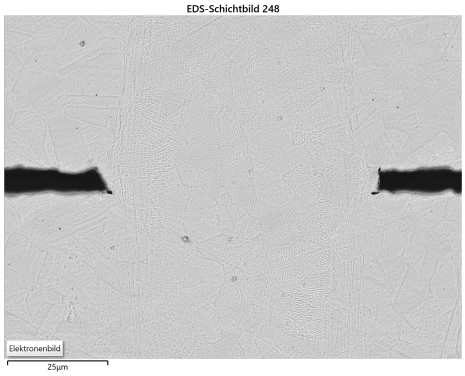

(a) Cross-sectional SEM

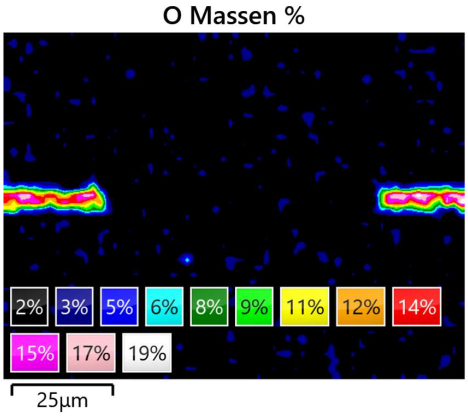

(b) EDX Oxygen Map

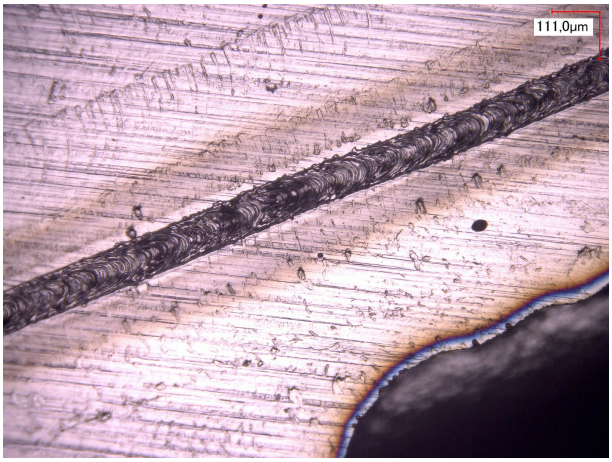

(c) Optical surface image

Figure 30 – SEM, EDX, and surface microscopy for (Mask 2, V3, 12 L/min)

Source: Author

The unshielded reference sample for weld path 1, welded with only bottom-side gas delivery, Figure 31, displays a highly porous microstructure. While the weld pool seen in the SEM image (Figure 31a) is mostly composed of equiaxed grains, it is compromised by a significant number of visible linear discontinuities. The most prominent feature is the great number of pores, which is substantially higher than in any of the shielded samples. The EDX map (Figure 31b) confirms that this widespread porosity is directly associated with a high concentration of oxygen.

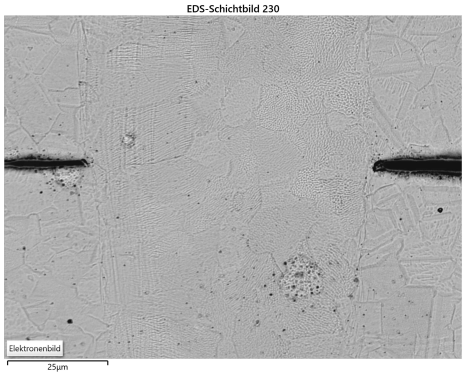

(a) Cross-sectional SEM

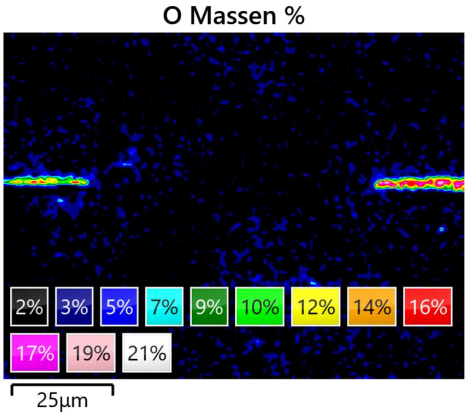

(b) EDX Oxygen Map

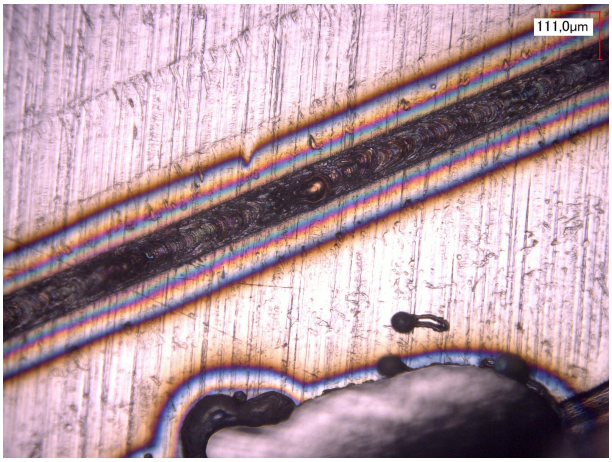

(c) Optical surface image

Figure 31 – SEM, EDX, and surface microscopy for weld with no mask, path 1

Source: Author

For weld path 2 of the unshielded reference sample, Figure 32, the microstructure is of surprisingly good quality. The SEM image (Figure 32a) shows clearly defined boundaries between the weld pool and the base material. The structure is mostly composed of equiaxed grains and is largely free of significant defects, with no visible linear discontinuities. Only a few pores and very few small, grey patches are identifiable. The corresponding EDX map (Figure 32b) indicates that these few pores and grey patches are the locations with a higher concentration of oxygen.

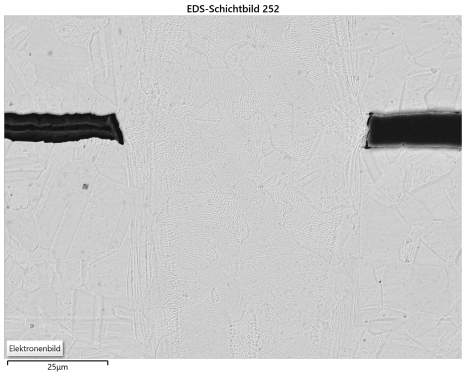

(a) Cross-sectional SEM

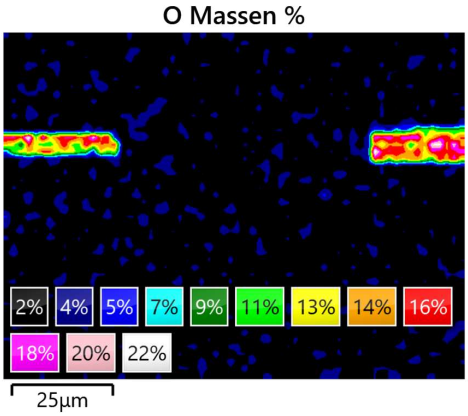

(b) EDX Oxygen Map

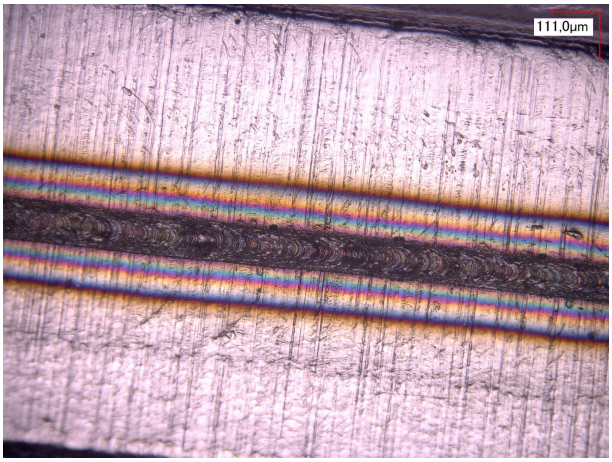

(c) Optical surface image

Figure 32 – SEM, EDX, and surface microscopy for weld with no mask, path 2

Source: Author

The cross-sectional analysis revealed that the Version 3 design, specifically Mask 2 operating at 12 L/min, produced the most structurally sound weld, which was homogeneous and remarkably free of defects. However, the results also indicate that while superior, the Version 3 design has not achieved a complete solution to oxidation. Optical microscopy still identified residual oxidation at the edges of the weld paths, suggesting that gas coverage remains imperfect in these localized areas. Furthermore, performance was not entirely uniform even within the final design, as Mask 1 and Mask 2 of Version 3 yielded different quality welds under the same optimal flow conditions.

Also, the cross-sectional analysis is limited by the number of samples and the specific locations chosen for examination. Future work should consider a more extensive sampling strategy to capture a broader range of weld conditions and geometries, as well as additional flow rates to further refine the understanding of gas shielding effectiveness.

6 Final considerations

The comprehensive analysis and experimental validations conducted throughout this project demonstrated significant improvements in gas shielding performance during the laser welding of metallic bipolar plates. Each iterative modification, informed by computational simulations and practical experimentation, contributed incrementally to more effective gas shielding, noticeably reducing oxidation and improving weld quality. The final optimized geometry in Iteration 3 showed the most substantial improvements, particularly at moderate gas flow rates, effectively achieving enhanced gas distribution and minimized oxidation.

However, despite these advancements, complete uniformity in gas coverage was not fully realized, notably at the outlet edges and extremities of the weld paths. An essential finding from the experiments was the noticeable discrepancy between the left and right, as well as top and bottom sides of the welds, despite geometric symmetry. These differences highlight the significant influence of the external gas feeding arrangement on the shielding effectiveness.

Alterations in the gas supply system between different welding sessions further validated this influence, emphasizing the importance of carefully managing and standardizing the gas delivery system alongside internal design enhancements. Figure 33 demonstrate this variability. Both figures are taken from the same position in the weld with 12 L/m in version 3, but the gas supply system layout, the position and length of the tubes, was altered between the two sessions, leading to significant differences in the gas shielding performance.

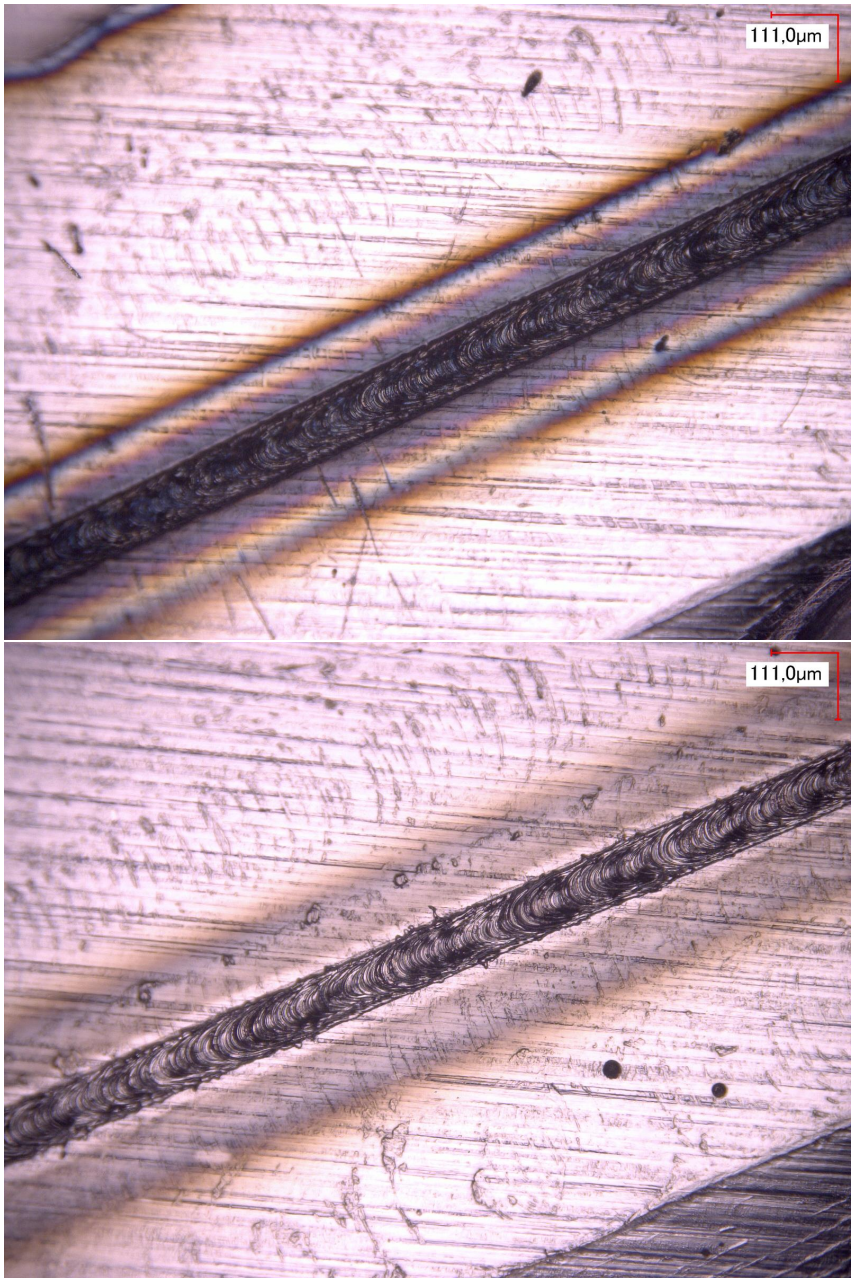

Figure 33 – Variability in gas shielding performance due to changes in the gas supply system.

Source: Author

Moreover, Mask 2 consistently outperformed Mask 1, indicating inherent advantages in its geometric configuration related to improved flow dynamics and gas retention capabilities. These observations suggest that even minor geometric variations significantly affect gas flow behavior and resultant weld quality, underscoring the importance of meticulous design considerations.

While the iterative design improvements markedly enhanced gas shielding effectiveness, particularly evident in the superior performance of Mask 2 V3 at optimized flow

conditions, further refinements in gas distribution uniformity and external gas feeding consistency remain critical areas for achieving an ideal and consistently reliable welding performance.

6.1 Future Work

While the current study has demonstrated a substantial improvement in gas shielding design for laser welding of bipolar plates, the results also reveal several promising avenues for future exploration and refinement. These directions span both practical enhancements and advanced research methodologies, offering pathways to achieve even greater control over oxidation and weld quality.

A critical first step would be to standardize and control the external gas feeding system, which was identified as a major source of variability; this could be achieved by implementing a rigid manifold to replace the flexible tubing and exploring the integration of individual mass flow controllers.

In parallel with such a system-level improvement, further targeted refinement of the successful Mask 2, Version 3 geometry is recommended, with a focus on modifying the outlet peripheries to eliminate the residual oxidation observed in the optical analysis. To guide these potential modifications and provide quantitative feedback on their effectiveness, it would be beneficial to implement enhanced validation methods such as Schlieren imaging, (SETTLES, 2001), and in-situ oxygen sensors. Only after such optimizations are validated could further work explore alternative high-temperature additive manufacturing materials to enhance the fixture's long-term durability.

Bibliography

ASHGRIZ, N.; MOSTAGHIMI, J. Fluid flow handbook. *Fluid flow handbook*, n. 1, 2002. Cited in page 22.

BORUP, R.; VANDERBORGH, N. Design and testing criteria for bipolar plate materials for pem fuel cell applications. *Materials Research Society Symposium - Proceedings*, v. 393, p. 151–155, 1995. Cited in page 12.

CAMPBELL, S. et al. A computational fluid dynamic analysis of the effect of weld nozzle geometry changes on shielding gas coverage during gas metal arc welding. *Journal of Manufacturing Science and Engineering*, n. 135, 2013. Cited 5 times in pages 20, 23, 28, 29, and 32.

CARRETTE, L.; FRIEDRICH, K. A.; STIMMING, U. Fuel cells: Principles, types, fuels, andapplications. *ChemPhysChem*, n. 4, 2000. Cited in page 9.

CHO, S.-M. et al. Effect of nozzle clogging on surface flow and vortex formation in the continuous casting mold. *AIST*, p. 85 – 95, 2012. Cited in page 25.

DU, W. et al. Laser micro-welding of stainless steel foil: Welding mode, microstructure and corrosion properties. *Optics and Laser Technology*, n. 161, 2023. Cited 3 times in pages 18, 19, and 20.

GANDHI, T. *Microeletronics Failure Analysis*. [S.l.]: ASM International, 2019. Cited in page 21.

HERMANN, A.; CHAUDHURI, T.; SPAGNOL, P. Bipolar plates for pem fuel cells:a review. *International Journal of Hydrogen Energy*, n. 30, p. 1297–1302, 2005. Cited 4 times in pages 10, 13, 15, and 16.

INC., A. *ANSYS Fluent Theory Guide*. [S.l.]: ANSYS, Inc., 2023. Cited in page 22.

KATAYAMA, S. *Handbook of laser welding technologies*. [S.l.]: Woodhead Publishing, 2013. Cited 3 times in pages 17, 18, and 23.

KOU, S. *Welding Metallurgy*. [S.l.]: Wiley, 2003. Cited in page 23.

MEHTA, V.; COOPER, J. Review and analysis of pem fuel cell design and manufacturing. *Journal of Power Sources*, p. 32–53, 2003. Cited in page 12.

MIRIKAR, D. et al. Flow characterization of a submerged inclined impinging pulse jet. *Physics of Fluids*, n. 36, 2024. Cited in page 30.

MUNSON, B. R. *Fundamentals of fluid mechanics*. [S.l.]: Hoboken, NJ Wiley, 2010. Cited 4 times in pages 23, 29, 33, and 38.

NEWBURY, D. E.; RITCHIE, N. W. M. Is scanning electron microscopy/energy dispersive x-rayspectrometry (sem/eds) quantitative? *Scanning*, n. 35, p. 141–168, 2013. Cited in page 21.

ROY, S. et al. An experimental and numerical study of heat transfer off an inclined surface subject to an impinging airflow. *International Journal of Heat and Mass Transfer*, n. 45, p. 1615 – 1629, 2002. Cited in page 30.

SCHRICKER, K.; BAUMANN, A.; BERGMANN, J. P. Local shielding gas supply in remote laser beam welding. *Journal of Manufacturing and Materials Processing*, n. 139, 2021. Cited 2 times in pages 25 and 28.

SETTLES, G. S. *Schlieren and Shadowgraph Techniques: Visualizing Phenomena in Transparent Media*. [S.l.]: Springer, 2001. Cited in page 68.

SHIRINZADEH-DASTGIRI, M. et al. Metallurgical investigations and corrosion behavior of failed weld joint in aisi 1518 low carbon steel pipeline. *Engineering Failure Analysis*, n. 53, p. 78–96, 2015. Cited in page 21.

SONG, Y. et al. Review on current research of materials, fabrication and application for bipolar plate in proton exchange membrane fuel cell. *International Journal of Hydrogen Energy*, p. 29832–29847, 2020. Cited in page 13.

STEEN, . J. M. W. M. *Laser Material Processing*. [S.l.]: Springer, 2010. Cited in page 18.

TAWFIK, H.; HUNG, Y.; MAHAJAN, D. Metal bipolar plates for pem fuel cell—a review. *Journal of Power Sources*, n. 163, p. 755–767, 2007. Cited 4 times in pages 11, 13, 15, and 16.

WANG, H.; TURNER, J. A. Ferritic stainless steels as bipolar plate material for polymer electrolyte membrane fuel cells. *Journal of Power Sources*, p. 193–200, 2004. Cited in page 15.

WOLTERSDORF, J. et al. Interlayer microstructure and bonding behaviourof ultrasonic-welded aluminium oxide/aluminium joints. *physica status solidi (a)*, n. 150, p. 307 – 317, 1995. Cited 2 times in pages 21 and 22.

XIONG, K. et al. Modeling, design, materials and fabrication of bipolar plates for proton exchange membrane fuel cell: A review. *Applied energy*, 2021. Cited in page 11.

YANG, Y.; LOU, X.; GE, G. Performance optimizing strategies for pemfc and electrode materials. *Highlights in Science, Engineering and Technology*, n. 106, p. 666 – 672, 2024. Cited in page 24.

ANNEX A – Mechanical Drawings of Gas Shielding Structures

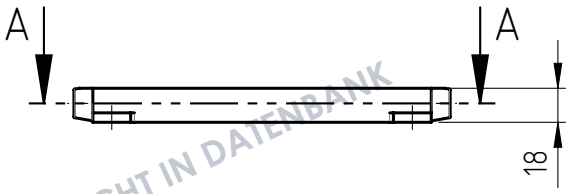

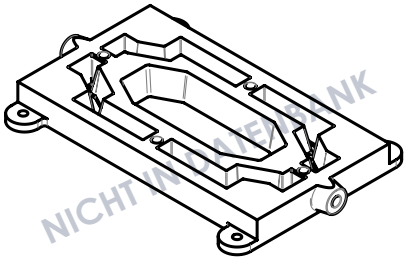

A–A

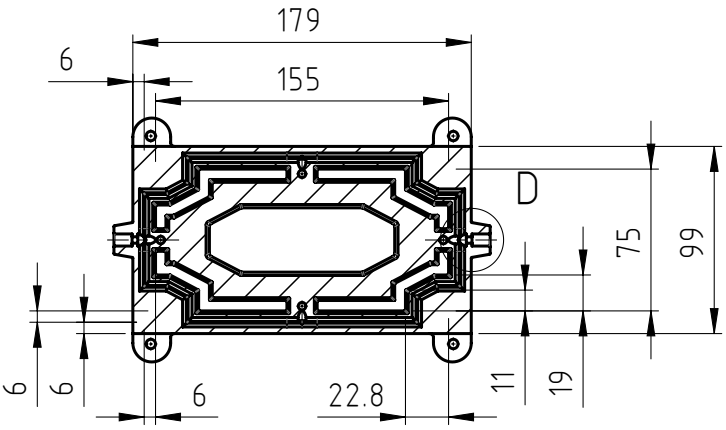

C–C

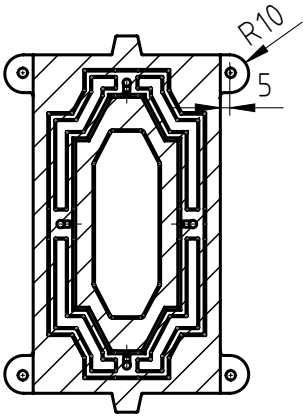

B–B

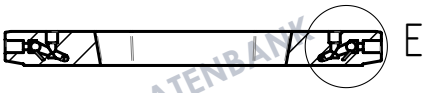

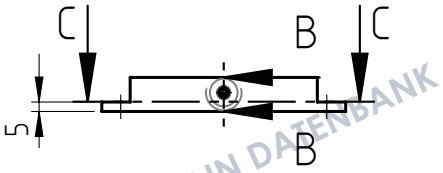

D (1 : 1)

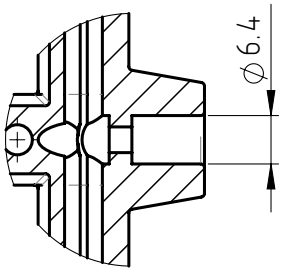

E (1 : 1)

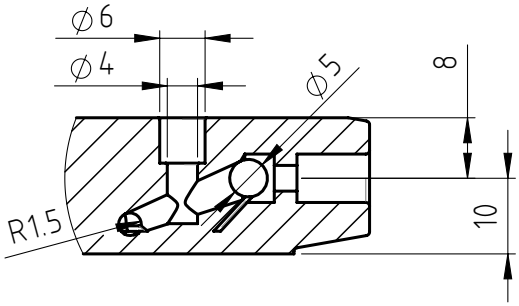

Size ISO 14405 E | Allgemein-Toleranzen DIN ISO 2768 - - E Oberflächenangaben DIN EN ISO 1302 | Kanten DIN ISO 13715	Vertraulich / Confidential	
Blattmaßstab 1:4	Gewicht 0.000 g/kg	
3D gesp. 19/07/2024 10:51:39 sgp 2D gesp. 06/06/2025 13:29:22 khj-bp	Blatt 1 von 1	
2D-Titel / Rev. Mask 1 V1 /		
Benennung EP / Konfig. /		
Werkstoff Halbzeug Material <not specified>		
Benennung / Nummer - NICHT IN DATENBANK - –		
Ursprung. Dateiname		

Rev	3D-Änderung	Name	Datum

Fraunhofer IPT | WZL | RWTH AACHEN UNIVERSITY

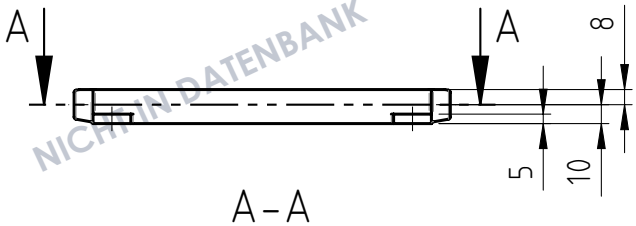

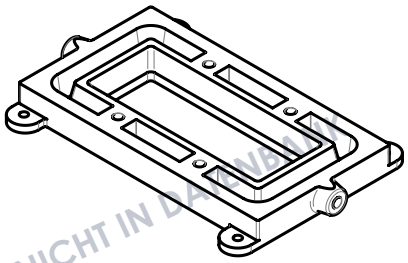

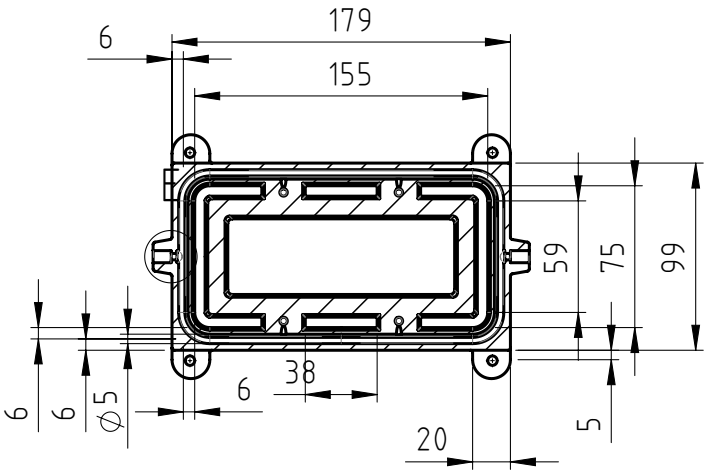

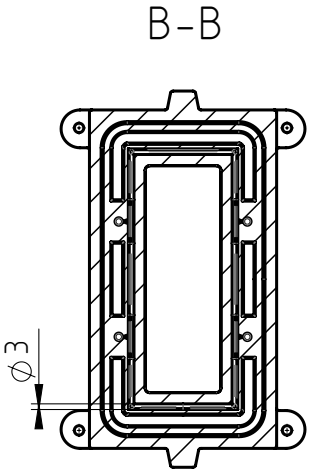

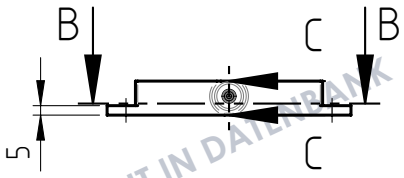

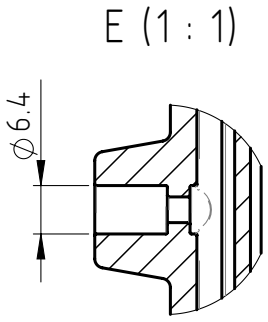

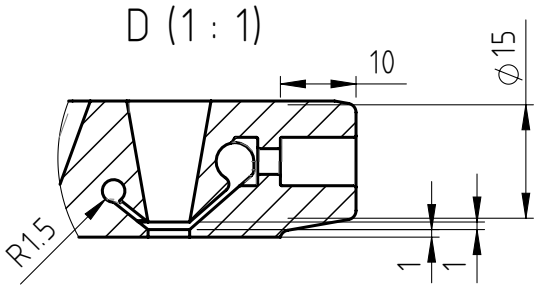

Size ISO 14405 E | Allgemein-Toleranzen DIN ISO 2768 - - E Oberflächenangaben DIN EN ISO 1302 | Kanten DIN ISO 13715	Vertraulich / Confidential	
Blattmaßstab 1:4	Gewicht 0.000 g/kg	
3D gesp. 19/07/2024 10:51:40 sgp 2D gesp. 07/06/2025 12:39:34 khj-bp	Blatt 1 von 1	
2D-Titel / Rev. Mask 2 V1 /		
Benennung EP / Konfig. /		
Werkstoff Halbzeug Material <not specified>		
Benennung / Nummer - NICHT IN DATENBANK -		
Urspr. Dateiname -		

Rev	3D-Änderung	Name	Datum

Fraunhofer IPT | WZL | RWTH AACHEN UNIVERSITY

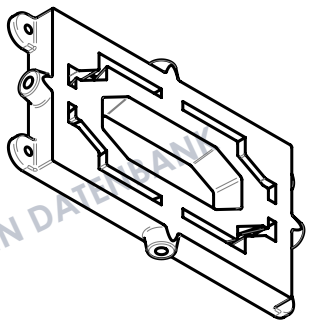

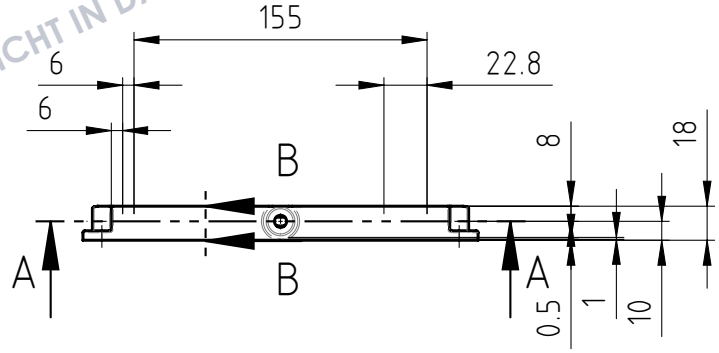

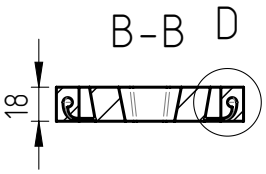

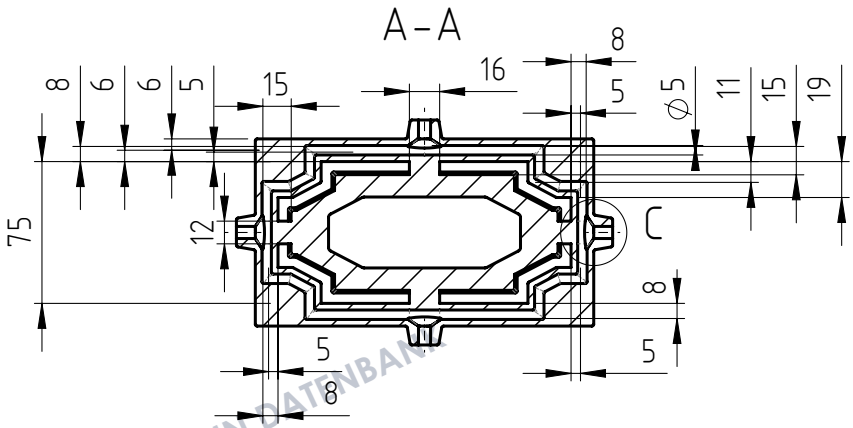

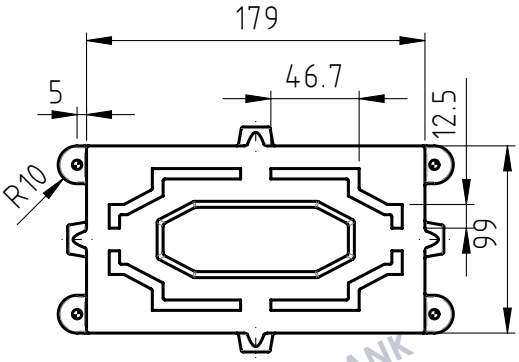

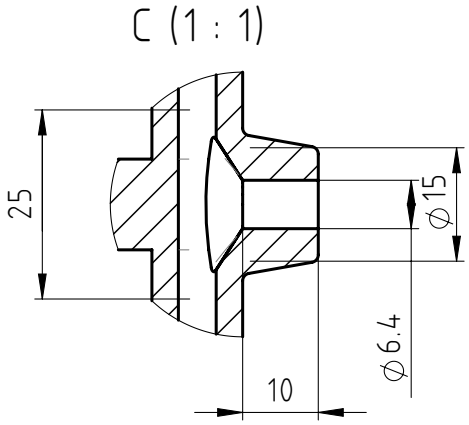

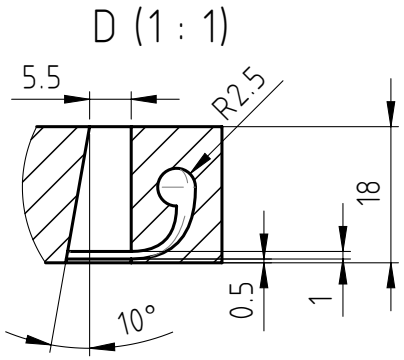

Size ISO 14405 E | Allgemein-Toleranzen DIN ISO 2768 - - E Oberflächenangaben DIN EN ISO 1302 | Kanten DIN ISO 13715		Vertraulich / Confidential	
Blattmaßstab 1:4		Gewicht 0.000 g/kg	
3D gesp. 15/04/2025 14:25:33 khj-bp 2D gesp. 07/06/2025 12:47:03 khj-bp		Blatt 1 von 1	
2D-Titel / Rev. Mask 1 V2 /			
Benennung EP / Konfig. /			
Werkstoff Halbzeug Material <not specified>			
Benennung / Nummer - NICHT IN DATENBANK - –			
Ursprung. Dateiname			

Rev	3D-Änderung	Name	Datum

Fraunhofer IPT | WZL | RWTH AACHEN UNIVERSITY

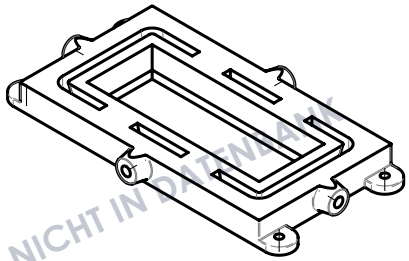

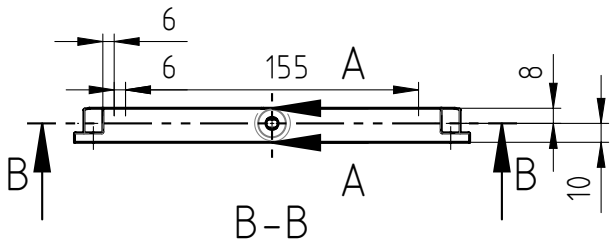

B-B

A-A

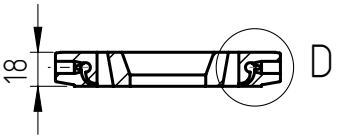

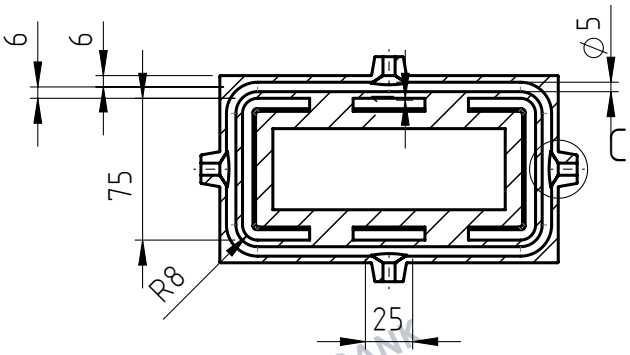

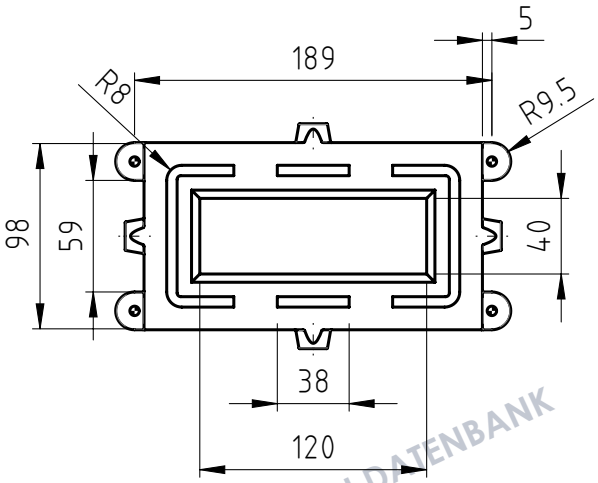

C (1 : 1)

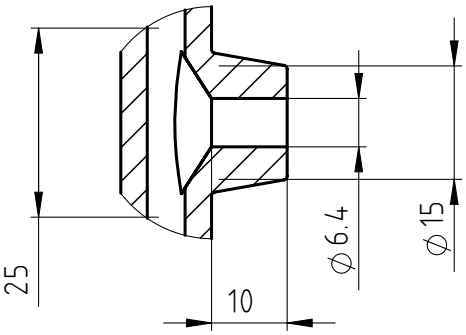

D (1 : 1)

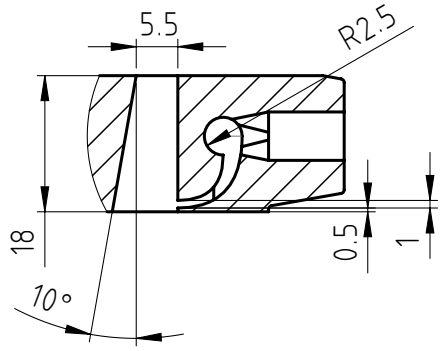

Size ISO 14405 E | Allgemein-Toleranzen DIN ISO 2768 - - E Oberflächenangaben DIN EN ISO 1302 | Kanten DIN ISO 13715		Vertraulich / Confidential	
Blattmaßstab 1:4		Gewicht 0.000 g/kg	
3D gesp. 15/04/2025 09:46:20 khj-bp 2D gesp. 07/06/2025 12:49:53 khj-bp		Blatt 1 von 1	
2D-Titel / Rev. Mask 2 V2 /			
Benennung EP / Konfig. /			
Werkstoff Halbzeug Material <not specified>			
Benennung / Nummer - NICHT IN DATENBANK - –			
Ursprung. Dateiname			

Rev	3D-Änderung	Name	Datum

Fraunhofer IPT | WZL | RWTH AACHEN UNIVERSITY

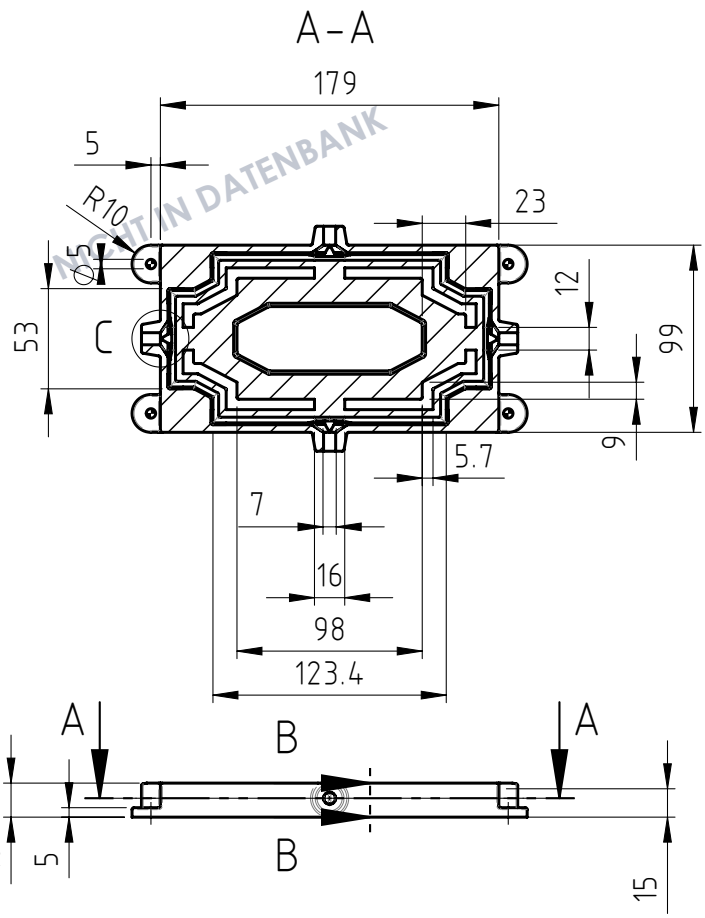

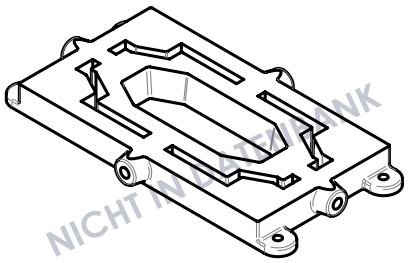

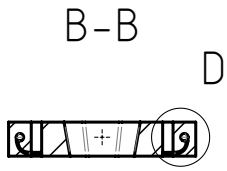

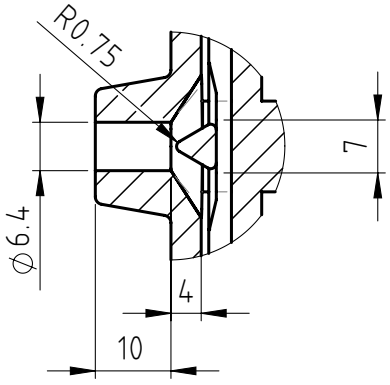

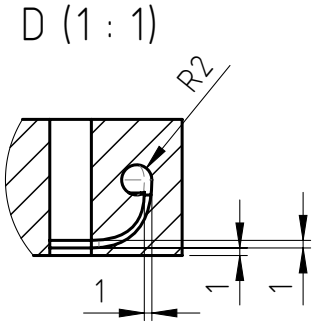

Size ISO 14405 E | Allgemein-Toleranzen DIN ISO 2768 - - E Oberflächenangaben DIN EN ISO 1302 | Kanten DIN ISO 13715		Vertraulich / Confidential	
Blattmaßstab 1:4		Gewicht 0.000 g/kg	
3D gesp. 30/04/2025 16:17:36 khj-bp 2D gesp. 06/06/2025 15:55:25 khj-bp		Blatt 1 von 1	
2D-Titel / Rev. Mask 1 V3 /			
Benennung EP / Konfig. /			
Werkstoff Halbzeug Material <not specified>			
Benennung / Nummer - NICHT IN DATENBANK - –			
Urspr. Dateiname			

Rev	3D-Änderung	Name	Datum

Fraunhofer IPT | WZL | RWTH AACHEN UNIVERSITY

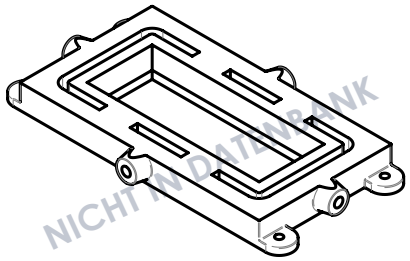

A-A

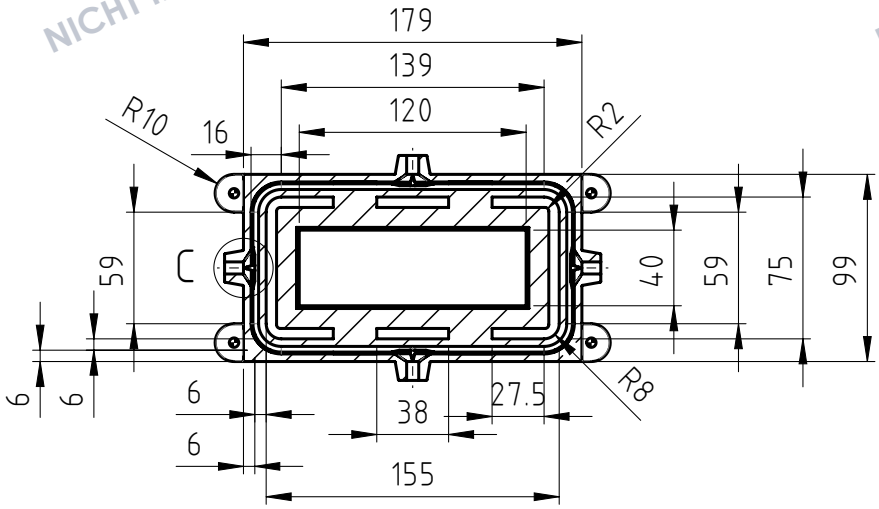

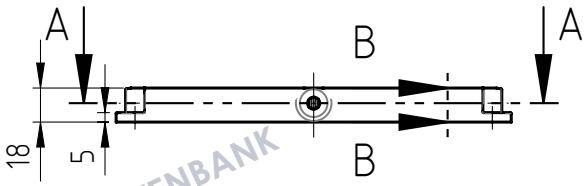

B-B

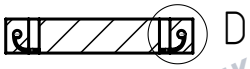

C (1 : 1)

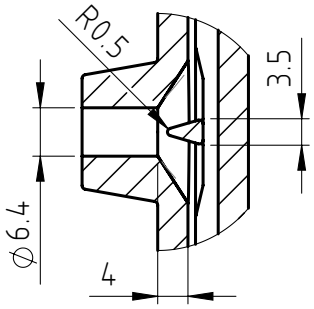

D (1 : 1)

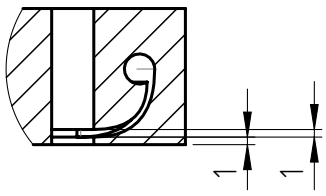

Size ISO 14405 E | Allgemein-Toleranzen DIN ISO 2768 - - E Oberflächenangaben DIN EN ISO 1302 | Kanten DIN ISO 13715		Vertraulich / Confidential	
Blattmaßstab 1:4		Gewicht 0.000 g/kg	
3D gesp. 31/05/2025 12:53:37 khj-bp 2D gesp. 07/06/2025 13:01:54 khj-bp		Blatt 1 von 1	
2D-Titel / Rev. Mask 2 V3 /			
Benennung EP / Konfig. /			
Werkstoff Halbzeug Material <not specified>			
Benennung / Nummer - NICHT IN DATENBANK - -			
Ursprung. Dateiname			

Rev	3D-Änderung	Name	Datum

Fraunhofer IPT | WZL | RWTH AACHEN UNIVERSITY